



# Crystallization and melting of bulk polymers: New observations, conclusions and a thermodynamic scheme

Gert Strobl

*Institut für Physik, Albert-Ludwigs-Universität Freiburg, 79104 Freiburg, Germany*

Received 5 August 2005; received in revised form 19 December 2005; accepted 19 January 2006

Available online 29 March 2006

## Abstract

New findings during the last decade have triggered a reconsideration of the foundations of polymer crystallization. The article reviews the new experimental results, points to some straightforward conclusions and also presents a novel thermodynamic scheme developed on the basis of the observations. The expansion of knowledge is due to the introduction of novel techniques: in situ atomic force microscopy, modulated and high speed calorimetry, microbeam X-ray scattering, combinations of standard techniques in simultaneous measurements, or the use of new evaluation procedures in scattering experiments and spectroscopy. This is demonstrated by a selection of important and clear-cut experimental results. Attention is restricted to the crystallization (from a quiescent melt or an isotropic glass) and melting of homopolymers and related statistical copolymers in bulk.

© 2006 Elsevier Ltd. All rights reserved.

*Keywords:* Polymer crystallization; Crystal melting; Recrystallization; Crystal size; Mesomorphic phases; Crystallinity

## Contents

|   |     |
|---|-----|
| 1. Introduction   | 399 |
| 2. Local observations of nucleation and growth              | 400 |
| 2.1. In situ AFM studies                                    | 400 |
| 2.2. Microbeam X-ray scattering                             | 402 |
| 3. Crystallization isotherms                                | 403 |
| 3.1. Growth- and filling-dominated kinetics                 | 403 |
| 3.2. Melt memory effects                                    | 405 |
| 4. Crystal thickness  | 407 |
| 4.1. Time dependent SAXS experiments                        | 407 |
| 4.2. Polyethylene: Crystal thickening                       | 408 |
| 5. Granular substructure of lamellae                        | 409 |
| 6. Crystal stability variations                             | 410 |
| 6.1. Thermal response                                       | 411 |
| 6.2. Stabilization during crystallization                   | 412 |
| 7. Crystallization line and melting line                    | 414 |
| 7.1. $T_c$ - $d_c$ - $T_f$ relationships                    | 414 |
| 7.2. Effects of co-units, diluents, blending and molar mass | 416 |
| 8. Recrystallization processes                              | 419 |

*E-mail address:* [strobl@uni-freiburg.de](mailto:strobl@uni-freiburg.de)

|       |  |     |
|-------|--|-----|
| 9.    | Crystal thickness selection and melting properties . . . . .   | 421 |
| 9.1.  | Ostwald's rule applied to polymer crystallization . . . . .    | 422 |
| 9.2.  | A thermodynamic multiphase scheme . . . . .                    | 423 |
| 9.3.  | Some applications . . . . .                                    | 424 |
| 10.   | Metastable mesomorphic phases . . . . .                        | 426 |
| 10.1. | The hexagonal phase of polyethylene . . . . .                  | 427 |
| 10.2. | The trans mesophase of <i>s</i> -polypropylene . . . . .       | 429 |
| 11.   | Orientation by magnetic fields . . . . .                       | 431 |
| 12.   | Crystallinity . . . . .  | 432 |
| 13.   | Amorphous regions with reduced mobility . . . . .              | 434 |
| 13.1. | Characterization with mobility- sensitive techniques . . . . . | 435 |
| 13.2. | Surface crystallization and melting in polyethylene . . . . .  | 436 |
| 14.   | Growth rate . . . . .  | 438 |
|       | Acknowledgements . . . . .                                     | 439 |
|       | References . . . . .   | 439 |

## 1. Introduction

The understanding of crystallization and melting in bulk polymers is, for obvious reasons, a main issue in polymer physics: the questions which arise are of specific nature, different from those encountered in the crystallization of low molar mass systems, and the problems to be solved have technologic relevance; control of the mechanical properties of semicrystalline polymeric materials is more effective the better the understanding. When the fundamentals of the structure of semicrystalline polymers—stacks of layer-like crystallites with thicknesses in the nanometer-range embedded in an amorphous matrix—were revealed in the 1950s, considerations about the mechanism of formation of this structure started immediately. In the 1960s and 1970s, they became a major field of research and a focus of interest, discussed as a central topic in all structure oriented polymer conferences. One conference, organized by the Faraday Society in 1979 at Cambridge became famous as a climactic event [1]. It brought together in intense, often controversial discussions the different views and models developed by Fischer, Flory, Frank, Hoffman, Keller, Kovacs, Point and Wunderlich, to mention only some of many prominent contributors. An agreement among the scientists could not be reached, neither at this conference nor afterwards. However, in the years that followed, one approach gained the ascendancy—the one put forward by Hoffman, Lauritzen and their co-workers [2]. It was accepted and used in data evaluations by more and more workers, because it had a number of appealing features:

- The picture envisaged by the treatment—a crystalline lamella with an ordered fold surface and smooth lateral faces, growing layer by layer, with secondary

nucleation the rate determining step—is clear and easy to grasp.

- The theory yields a simple equation for the growth rate.
- As it appeared, the growth rate of the lamellae represents a well-defined property that can be easily measured, either by optical microscopy or globally with various techniques that probe the temporal development of the crystallinity.

The Hoffman–Lauritzen model was always confronted by criticism, but this did not hinder its success. Some points were taken up and led to modifications, but the foundation remained unchanged. By the late 1980s it was broadly applied. It became common procedure to represent the temperature dependence of measured growth rates and crystallization times with reference to the Hoffman–Lauritzen theory, search for the predicted ‘regime transitions’, and derive the parameters of the theory.

The impression of many in the scientific community that the mechanism of polymer crystallization was, in principle, understood, and the issue essentially settled, however was wrong. With the onset of the 1990s a reconsideration began, triggered by new experimental observations. In fact, the experimental basis of the Hoffman–Lauritzen theory had always been rather narrow. Putting the focus on growth rates alone, the basis of validation was growth rate measurements exclusively. The Hoffman–Lauritzen treatment includes several implications. In particular, it assumes:

- The lamellae grow by direct attachment of chain sequences from the melt onto essentially smooth lateral faces.
- The lamellar thickness is determined by the supercooling below the equilibrium melting point—given

by the Gibbs–Thomson equation—apart from a minor correction which is necessary to provide a thermodynamic driving force.

These assumptions looked quite natural, and nobody would have questioned them without very good reasons. Such reasons, however, now arose:

- Keller and his co-workers, when crystallizing polyethylene at elevated pressures, observed the formation of crystals from a mesomorphic hexagonal phase and speculated that this may also happen under normal pressure [3].
- Kaji and co-workers interpreted scattering which arose before the appearance of the crystallites as indicating the buildup of a precursor phase in the first step of polymer crystallization [4], and Olmsted constructed a corresponding theory [5].
- Time and temperature-dependent small angle X-ray scattering experiments, at first carried out on syndiotactic polypropylene and related copolymers, contradicted the basic assumption of control of the lamellar thickness by the supercooling below the equilibrium melting point [6]. As it turned out, the lamellar thickness is determined by the supercooling below another temperature, which is always located above the equilibrium melting point. In addition, the thickness is not affected by the presence of co-units.

With these new observations fundamental questions about the mechanism of polymer crystallization were reopened.

The revival of this discussion, in a seemingly ‘mature’ field, initiated new activities. They brought new insights and new questions to which novel experimental tools could be applied. Of particular importance was the use of the atomic force microscope. All the previous time-dependent crystallization studies yielded only global values. The *in situ* observations, now possible with a resolution down to several nanometers, opened a completely new access. New insights also came from applying modulated and high speed calorimetry. With these novel techniques it became possible to extract, from the total heat flow, contributions associated only with reversible structure changes and also to study structure changes that take place within very short times. Also new were: the use of synchrotron radiation microbeams, which offered a spatial resolution of the superstructures in semicrystalline polymers—spherulites, fibers—down to the micrometer-range; the use of comparative techniques in the evaluation of temporal variations of infrared spectra during

crystallization processes; and simultaneous recordings of small angle and wide angle X-ray scattering patterns. Application of these new techniques has resulted in a major extension of knowledge in the field of polymer crystallization during the last decade.

This review will present a selection of such new experiments. In a wide and varied field like polymer crystallization, it can only be a selection rather than a compilation of all results. A selection always brings in weightings by the author and, due to knowledge limitations, arbitrary choices. Readers should be aware of this and also know that this review is not written by a neutral referee presenting different, sometimes controversial views for a comparison, but by one who is engaged in the field. In spite of that, throughout this article the attempt has been made to clearly separate observations, straightforward conclusions, and personal interpretations. To the latter class belongs in particular the thermodynamic scheme, which we have developed on the basis of our experiments, and which we now use for data evaluations and the discussion of various phenomena.

## 2. Local observations of nucleation and growth

Atomic force microscopy (AFM) is a most attractive tool for studies of polymer crystallization. It provides real-space images of local structures in time- and temperature- dependent *in situ* studies. The sample preparation method is easy, and achieved resolutions approach the 10 nm-range. In the following some selected examples are presented, dealing with:

- separate observations of nucleation, branching and splaying,
- observations of characteristic differences in the development of spherulites after homogeneous and heterogeneous nucleation,
- real-time observations of the sequential building up of spherulites and
- resolution of details of the boundary region of spherulites.

### 2.1. *In situ* AFM studies

Even if hot stages can be used for experiments at elevated temperatures, the best performance is still found at ambient temperature. Furthermore, studies of systems which crystallize slowly are also preferable. Chan, Li and co-workers prepared samples of poly(bis-phenol octane ether) (BA-C8), which allowed an investigation

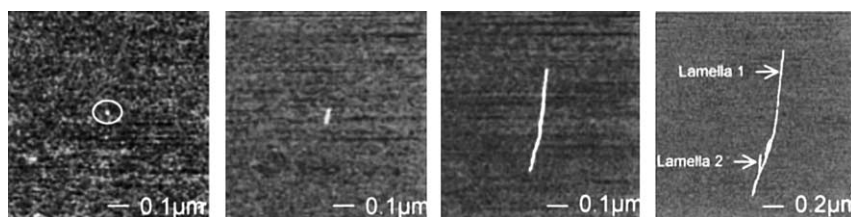


Fig. 1. BA-C8 crystallizing at 22 °C. AFM tapping-mode phase images of an embryo (left), one growing a primary lamella and the later development of branches (right). Reproduced with permission from Chan et al. [7]. Copyright (2002) American Chemical Society.

under such conditions. The polymer, synthesized by condensation polymerization, had a glass temperature of 10.5 °C and a melting point of 83.3 °C. Experiments were carried out on initially amorphous BA-C8 films with a thickness of 300 nm. Fig. 1 presents one of the results [7]. The dot in the left hand picture is a nucleus which subsequently develops into a single lamella. This starting event is a homogeneous nucleation. Indeed, the authors observed that not all dots that showed up at the beginning developed into lamellae. Some of them disappeared, i.e. disintegrated. As is shown in the picture on the right hand side, the first branches develop when the lamella reaches a size of the order of 1 μm.

If the branching is repeated for all the later starting lamellae, whenever they reach a length on the order of 1 μm, the embryo gradually develops into an object as is shown growing in Fig. 2. [8]. Finally, it will become a spherulite with a characteristic feature, a pair of ‘eyes,’ at its center.

If spherulites start from a heterogeneity by heterogeneous nucleation, a different growth pattern is observed, as is depicted in Fig. 3. In this case, several lamellae develop simultaneously, emanating from the surface of the heterogeneity. As a consequence, the growing object shows quasispherical symmetry from the very beginning. This differs from the initial anisotropy associated with a homogeneous nucleation, which is retained up to the end in the form and direction of the two eyes.

Bassett and co-workers introduced the notion of dominant and subsidiary lamellae in pioneering work carried out with a transmission electron microscope (TEM) [9]. The latter lamellae develop during a sequential buildup of spherulites. Spherulite growth proceeds by branching and splaying of the dominant lamellae, which provide the framework within which the subsequent growth of subsidiary lamellae occurs. Bassett arrived at this view when he examined the structures of developing spherulites at ambient temperature after quenching at different stages followed by surface etching to improve the contrast. Atomic force microscopy now enables an observation of the sequential buildup in real

time. Fig. 4 presents, as an example, a series of images obtained by Hobbs [10] during isothermal crystallization of polyethylene (PE) at 133 °C. The picture on the left hand side shows a few lamellae which have advanced with very rapid growth. As shown by the further pictures, this is followed by a retarded in-filling growth. The growth rate of the latter is obviously much slower. The observations are in full agreement with Bassett’s notion of dominant and subsidiary crystallites.

The sequential buildup of spherulites with a succession of rapidly growing dominant and slower growing in-filled secondary lamellae can also be visible at spherulite boundaries. An example again obtained by Hobbs et al. [11], is shown in Fig. 5; it also displays the effect of crystallization temperature. Experiments were carried out on poly(hydroxybutyrate-*co*-valerate) (PHBcV). A prerequisite was the use of an AFM that permits use of a special electronic control for fast



Fig. 2. In situ AFM recording of a crystallizing polyether (BA-C8 at 22 °C). AFM tapping-mode phase images of a homogeneously nucleated growing spherulite obtained at different times. Reproduced with permission from Li et al. [8]. Copyright (2003) Elsevier Science Ltd.

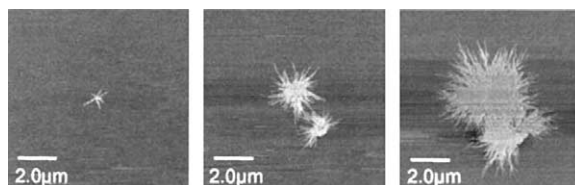


Fig. 3. In situ AFM recording of crystallizing BA-C8 (22 °C). Tapping-mode phase images of a heterogeneously nucleated growing spherulite obtained at different times. Reproduced with permission from Li et al. [8]. Copyright (2003) Elsevier Science Ltd.

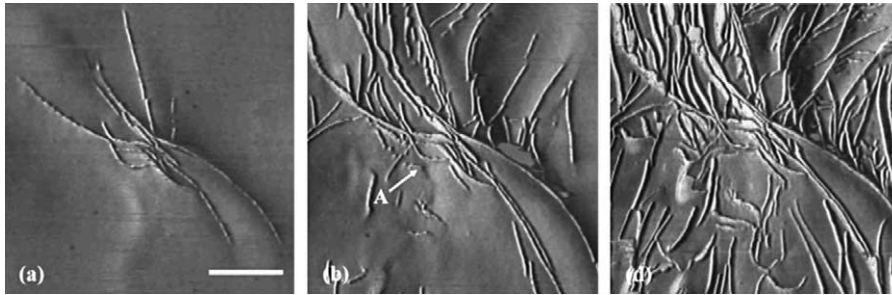


Fig. 4. PE crystallized at 133 °C: AFM tapping-mode phase images obtained after different times of development (scale bar: 1  $\mu\text{m}$ ). Reproduced with permission from Hobbs [10]. Copyright (2003) Springer-Verlag.

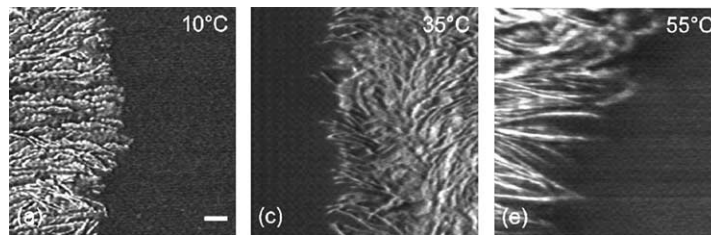


Fig. 5. P(HBcV): AFM tapping-mode phase images of the growth fronts of spherulites developing at different temperatures (scale bar: 100 nm). Reproduced with permission from Hobbs [11].

scanning; the higher growth rates at lower temperatures require such a tool. At the lowest crystallization temperature, 10 °C, the boundary looks rather sharp, but this changes at higher temperatures. At the highest temperature, one again clearly observes advancing dominant lamellae with a higher growth rate. The final density of lamellae is only reached at a certain distance behind the furthest forward crystallizing point. The observation can be explained by a reduction in the branching rate with an increase in the crystallization temperature.

## 2.2. Microbeam X-ray scattering

The existence of an extended boundary region through which the crystallinity varies is confirmed in experiments with another new tool, namely, micro-beam X-ray scattering which can be carried out with synchrotron radiation sources. Kolb, Riekel et al. [12] reported such an experiment conducted on isotactic polypropylene (iPP) and poly(vinylidene fluoride) (PVDF). The result is shown in Fig. 6. An X-ray beam with micrometer cross-section allows one to monitor structural changes when it is crossed by the boundary of a growing spherulite. There are no Bragg reflections as long as the micro-beam penetrates the amorphous region outside of the spherulite. Reflections start to appear when the boundary of the growing spherulite enters the

illuminated region. When the extension of the boundary region is more than 1  $\mu\text{m}$ , its profile becomes resolved. The figure presents a typical result obtained for iPP. It indicates that the width of the boundary region amounts to about 30  $\mu\text{m}$ . As is shown by the upper curve, the crystallinity profile of the boundary region can also be determined when growing spherulites are quenched to

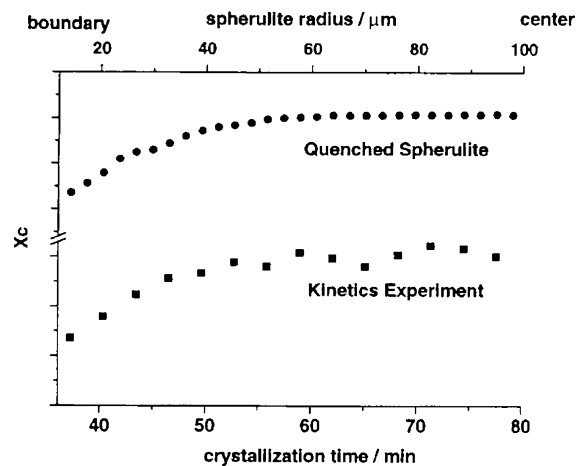


Fig. 6. iPP Crystallizing at 148 °C. Variation of the crystallinity through the boundary region of a growing spherulite as determined by a microbeam WAXS experiment in situ at the crystallization temperature and at room temperature after quenching. Reproduced with permission from Riekel et al. [12]. Copyright (2001) Elsevier Science Ltd.

room temperature. This stationary measurement yielded a similar profile.

### 3. Crystallization isotherms

Crystallization isotherms are recorded by applying various tools, the most popular being calorimetry, wide angle and small angle X-ray scattering, and dilatometry. There are now new experiments where two different tools are commonly used, either simultaneously or one after the other, in a comparison. Such combinations are of great value, because they allow discrimination between different factors acting together in the crystallization process.

It is a quite common procedure to evaluate data by fitting to the Avrami equation. The Avrami theory treats the growth of objects with a constant inner structure, which grow in one, two or three dimensions. As a matter of fact, a constant inner structure is not always found. As was discussed in the former section and demonstrated by AFM in situ observations, spherulites are often built up sequentially, starting with a rapid growth of dominant lamellae, which is then followed by an in-filling process. The Avrami equation does not deal with this often encountered situation. The data evaluation must therefore be put on a more general basis.

The dynamic range of all the standard tools is restricted. There are only rarely measurements which surpass two orders in the signal magnitude. This implies that for a spherulite with a normal final size of the order of a few micrometers, observations start only when it has already reached a size of several hundred nanometers. The initial stages of crystallization are thus outside the range of the standard measurements. However, there is an experimental tool with much higher sensitivity: measurement of the linear attenuation coefficient of light. Using that, one is able to encompass a dynamic range of more than four orders of magnitude.

In the following, three combined determinations of crystallization isotherms will be reviewed. They were conducted on syndiotactic polypropylene (sPP), poly(ethylene-co-octene) (PEcO) and poly( $\epsilon$ -caprolactone) (PeCL) which represent different cases of observed crystallization kinetics. The potential of time dependence measurements of the linear attenuation coefficient is demonstrated for a sample of PEcO.

#### 3.1. Growth- and filling-dominated kinetics

Fig. 7 presents crystallization isotherms of a commercial sPP obtained by small angle X-ray scattering (SAXS) and dilatometry (from Ref. [13]).

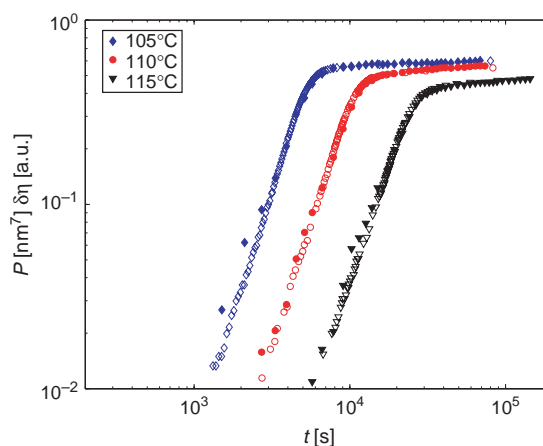


Fig. 7. sPP-Fina: crystallization isotherms as given by the time dependence of the Porod coefficient  $P$  (from SAXS, filled symbols) and of the density change  $\delta\rho$  (from dilatometry, open symbols). The initial slope indicates a kinetic power law  $P \propto \delta\rho \propto t^3$  [13].

The appropriate parameter to use in SAXS studies of crystallization kinetics is the Porod coefficient  $P$  defined as

$$P \propto (\Delta\rho_{ac})^2 O_{ac} \quad (1)$$

$P$  is determined by the amorphous–crystalline interface area per unit volume  $O_{ac}$  and the density difference  $\Delta\rho_{ac}$  between the crystals and the amorphous phase. At any time of the crystallization process,  $P$  can be derived from the asymptotic decay of the SAXS curves—homogeneity of the structure is not required. Multiplication by the crystal thickness  $d_c$  leads to

$$Pd_c \propto (\Delta\rho_{ac})^2 \phi_c \quad (2)$$

and thus to a property which includes the crystallinity  $\phi_c$ . On the other hand, dilatometry yields the change in the specific volume  $\delta v$  or the change in the global density  $\delta\rho$ , which can also be related to  $\Delta\rho_{ac}$  and  $\phi_c$  by

$$\delta v \propto d\rho \propto \Delta\rho_{ac} \phi_c \quad (3)$$

Fig. 7 uses a log–log plot to represent the time dependences  $P(t)$  and  $\delta\rho(t)$ . The power law for the initial development of crystallinity can be derived from the initial slope as

$$\phi_c \propto t^3 \quad (4)$$

This is the law expected for a constant growth rate of spherulites having a fixed inner structure. The agreement in the kinetics recorded in terms of  $P$  and in terms of  $\delta\rho$  confirms that the density in the growing lamellar crystallites does not change. The different functional

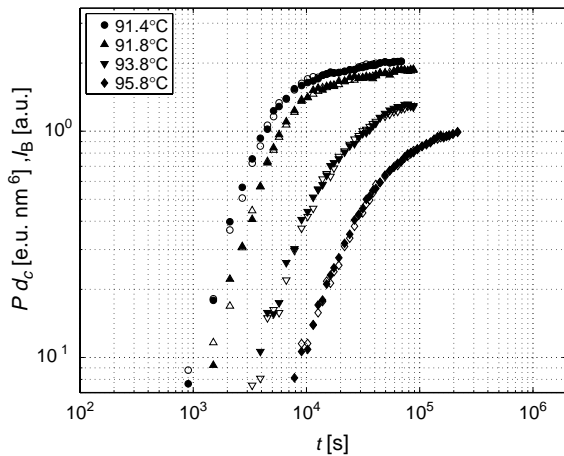


Fig. 8. SWAXS experiments on PEcO14: crystallization isotherms as given by the time dependence of the product  $Pd_c$  (open symbols) and by the change of the intensity of the 110-reflection  $I_B$  (filled symbols). The initial slopes indicate kinetic power laws  $Pd_c \propto I_B \propto t^\nu$  with  $\nu = 1.4$ – $1.6$  [14].

dependences of  $\delta\rho$  and  $P$  on  $\Delta\rho_{ac}$ —linear and quadratic, respectively—would result in different isotherms for  $P$  and  $\delta\rho$  if  $\Delta\rho_{ac}$  were to vary with time.

Fig. 8 depicts isotherms obtained in simultaneous small angle and wide angle X-ray scattering (SWAXS) experiments on PEcO14, a poly(ethylene-co-octene) with 14% per weight of octene co-units. The time dependence of the product  $Pd_c$  is compared with the time dependence of the intensity  $I_B$  of the 110-Bragg reflection. Both sets of isotherms coincide. Hence,  $\Delta\rho_{ac}$  is again a constant, i.e. the development of crystallinity is based on the growth of lamellar crystallites with constant density—there are no positive indications for intralamellar ordering processes within the timescale of the experiment. The power law found for the initial stages of crystallinity development differs from the first case: It is  $Pd_c \propto I_B \propto t^\nu$  with  $\nu = 1.4$ – $1.6$ . This result indicates that the crystallinity development is dominated by an in-filling process, rather than linear growth of spherulites. An open framework of dominant lamellae developed very rapidly in a first step, and the main part of the crystallization process is then the creation of subsidiary lamellae. Observations in a

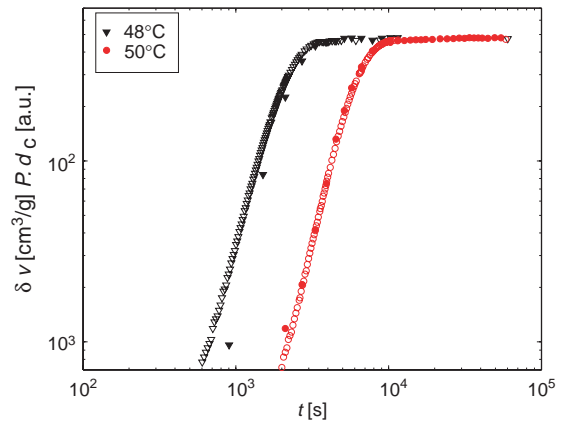


Fig. 10. PeCL: crystallization isotherms  $Pd_c(t)$  and  $\delta v(t)$  obtained by SAXS and dilatometry. The initial slope indicates a kinetic power law  $Pd_c \propto \delta v \propto t^4$  [13].

polarizing optical microscope (POM) confirmed this view. Fig. 9 depicts a typical series of images. The view field is completely filled with objects of essentially constant size, about  $5\ \mu\text{m}$ , and the crystallization process shows up as an increase in brightness. At the end, the objects have turned into spherulites. In addition to this major component, one growing spherulite shows up in the images which has a constant inner brightness from the beginning. One might speculate that the objects of constant size which become continuously filled started with a homogeneous nucleation. As discussed in the previous section, this leads at first to an open spherulite, which is subsequently filled. On the other hand, the few single spherulites which grow with constant brightness might have started from heterogeneities. Then many lamellae grow together and keep the spherulite filled from the very beginning.

A third possible case shows up in the experiment on PeCL depicted in Fig. 10 [13]. The isotherms  $Pd_c(t)$  and  $\delta v(t)$  determined by SAXS and dilatometry agree. Hence, again crystallites are growing with a constant inner density, but the initial growth law is peculiar. The slope corresponds to a power law  $Pd_c \propto \delta v \propto t^4$  and indicates that crystallization kinetics here is a result of

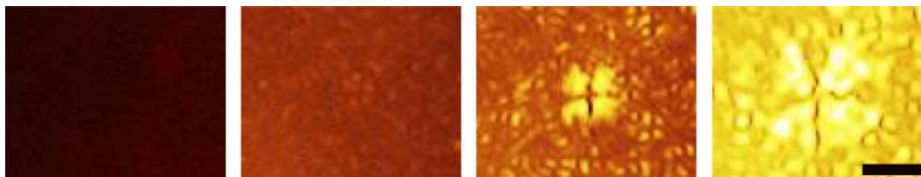


Fig. 9. PEcO14 crystallization at  $92^\circ\text{C}$ : POM images obtained at 0, 600, 1800 and 63000 s (from left to right); the scale bar has a length of  $10\ \mu\text{m}$  [14].

both the growth of spherulites and an accompanying in-filling process.

In all the presented experiments, recordings covered a range of only 1–2 orders of magnitude, which is typical for conventional techniques. A much higher sensitivity can be achieved in time-dependent measurements of  $\mathcal{A}$ , the linear attenuation coefficient of light. The attenuation of a laser beam passing through a platelike sample with a thickness  $D$  is given by the Lambert–Beer law as

$$I/I_0 = \exp(-\mathcal{A}D) \quad (5)$$

For  $\mathcal{A}$ , theory yields the expression [15,16]

$$\mathcal{A} \propto nR^4 (\Delta\rho_{\text{as}})^2 G \quad (6)$$

where  $n$  is the number density of growing objects,  $R$  is the spherulite radius,  $\Delta\rho_{\text{as}}$  is the difference between the mean density in the interior of the spherulites and the melt, and  $G$  represents an interference factor. During the initial stages of crystallization, when the volume fraction occupied by the spherulites is still low,  $G$  is equal to unity. For the case of growing sPP spherulites leading to the isotherms in Fig. 7 one expects  $\mathcal{A} \propto t^4$ , which was indeed found [15]. Fig. 11 shows the result of  $\mathcal{A}$  measurements for PEcO14 [16], the sample that gave the SWAXS isotherms of Fig. 8. The measurements now extend over more than four orders of magnitude. The isotherm for the highest temperature follows a power law  $\mathcal{A} \propto t^{2.5}$ , again indicative of the dominance of the in-filling processes; the time dependence of  $\mathcal{A}$  here relates to an increase of  $\Delta\rho_{\text{as}}$  only.

### 3.2. Melt memory effects

If a semicrystalline polymer is melted and then recrystallized, memory effects may occur. It is then found that the time required for the second crystallization varies with the temperature of the melt and the time during which the sample is kept in the molten state. Crystallization times tend to decrease when the melt temperature is lowered and the period of melting is shortened [17]. Memory effects are commonly explained by assuming persistence of nuclei in the melt. This is a reasonable explanation if the shape of the isotherms is retained, because a variation in the number of growing spherulites leads only to a shift of the curves along the  $\log t$ -axis. The two experiments addressed in the following indicate other changes.

Fig. 12 presents various isotherms measured for a commercial sPP using a dilatometer [18]. The decrease in the specific volume for a fixed crystallization temperature,  $T_c = 105^\circ\text{C}$ , and various temperatures  $T_m$  of the melt is presented in log–log plots. The sample was always kept for 20 min at  $T_m$  before it was rapidly cooled to the crystallization temperature. For melt temperatures above  $161^\circ\text{C}$  the same result was always obtained, whereas for temperatures below this critical value the crystallization isotherms vary. The shape of the curve is thereby altered. For high melt temperatures the initial increase of the crystallinity is that of filled spherulites with a constant growth rate ( $v_0 - v \propto t^3$ ). For lower melt temperatures the power law changes, and for the lowest temperatures  $v_0 - v \propto t^5$  is found. Here, the

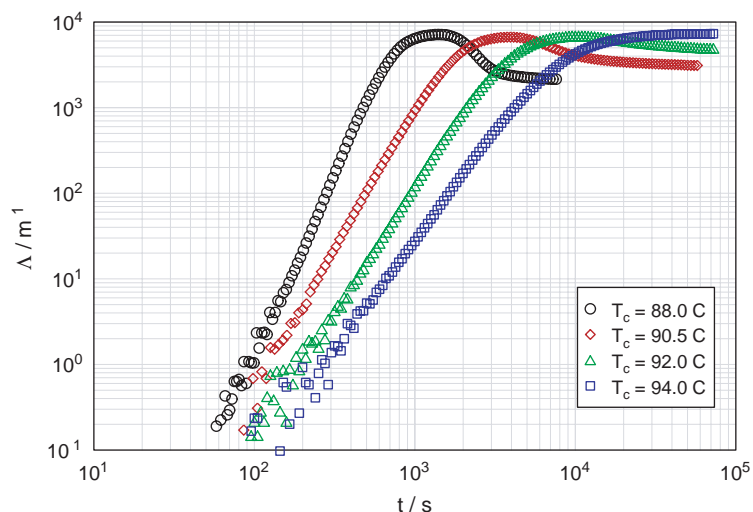


Fig. 11. PEcO14 Crystallized at various temperatures: isotherms given by the time dependence of the light attenuation coefficient  $\mathcal{A}$  [16].

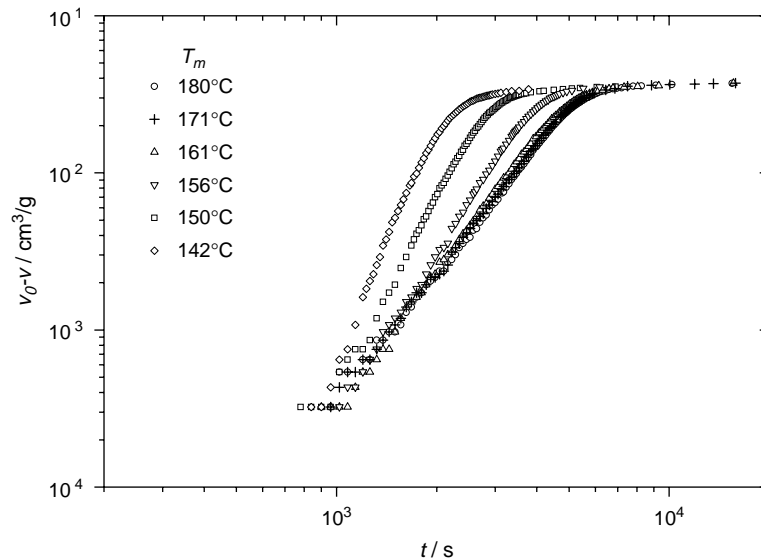


Fig. 12. SPP-Fina: kinetics of crystallization at  $T_c = 105\text{ }^\circ\text{C}$  as observed with a dilatometer for different temperatures  $T_m$  of the melt prior to cooling ( $v$ , specific volume;  $v_0$ , specific volume of the melt at  $T_c$ ) [18].

growth is not only faster, but is accompanied by an in-filling process.

Pronounced melt memory effects were also found for PEcO14, the sample with crystallization kinetics dominated by the in-filling processes (compare Figs. 8 and 9). Fig. 13 reproduces dilatometric isotherms, again measured for a constant crystallization temperature,  $T_c = 93\text{ }^\circ\text{C}$ , and various temperatures of the melt (from Ref. [19]). One observes a general shift to shorter times with decreasing  $T_m$  and two noteworthy features:

- Isotherms start with a power law close to  $\phi_c \propto t$ , which indicates a first order process for the creation of crystallites.
- Independent of the chosen melt temperature all isotherms finally end up at the low  $T_m$  limiting curve.

The latter may therefore be assigned to the growth of initially nearly empty objects, for example, open spherulites composed of a few dominant lamellae only. Then, these are filled with subsidiary crystallites, and the filling rate changes with the temperature of the melt.

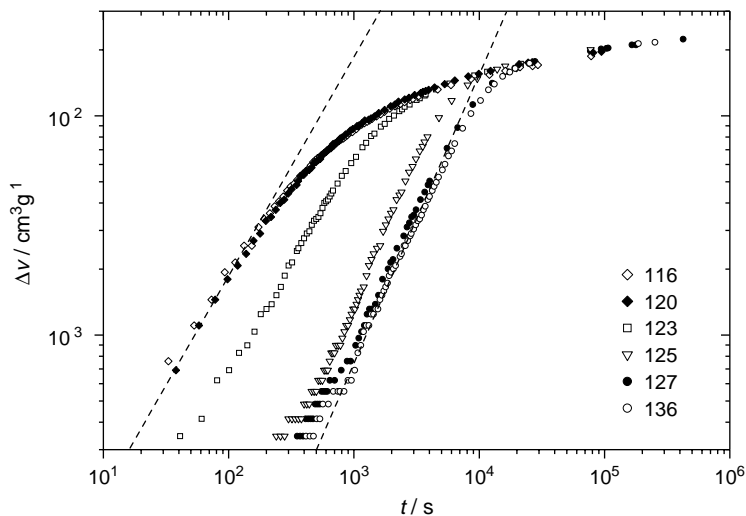


Fig. 13. PEcO14: dilatometric crystallization isotherms,  $\Delta v(t) = v_0 - v(t)$ , for  $T_c = 93\text{ }^\circ\text{C}$  and the indicated melt temperatures [19].

#### 4. Crystal thickness

For many years, crystallization and melting of statistical copolymers were treated differently from the case of homopolymers. Workers in the field took up Flory's idea to essentially treat copolymers like a system of oligomers with a molar mass distribution corresponding to the copolymer sequence length distribution [20]. In this view, crystallization is described as an equilibrium process associated with segregation of sequences of different length. Isothermal crystallization starts with the formation of thick crystals composed of the longest sequences, then continues with thinner crystals and ends with the formation of crystallites having the minimum thickness necessary to keep them stable in the surrounding melt. In a subsequent heating process, the crystallites melt in reverse order. With this approach two completely different concepts existed in the field of crystallizing polymers: Hoffman and Lauritzen's kinetic theory—applied to homopolymers—and Flory's equilibrium treatment of copolymer systems.

Time dependent SAXS experiments and AFM scans carried out in situ at the crystallization temperature have the potential to detect segregation processes. They have been carried out for various systems, and the outcome of several investigations appears quite clear: in both cases, homopolymers and statistical copolymers, isothermal crystallization leads to crystals with uniform thickness. Indications of segregation were not found. The only exception is polyethylene where thickening processes in the crystalline state—made possible by the activity of the  $\alpha$ -process—ultimately produces a thickness distribution. A few examples follow.

##### 4.1. Time dependent SAXS experiments

In recent years, SAXS curves of semicrystalline polymers were more and more evaluated via the interface distance distribution function (IDF) [21,22]. The latter, denoted  $K''(z)$ , follows from the scattering curve  $I(q)$  by applying a Fourier transformation:

$$K''(z) \propto \int_0^{\infty} \left[ \lim_{q \rightarrow \infty} (q^4 I(q)) - q^4 I(q) \right] \cos(qz) dq \quad (7)$$

Here,  $q$  denotes the scattering vector,  $q = 4\pi \sin \theta / \lambda$ , with  $\theta$  the Bragg angle and  $\lambda$  the wavelength. For crystallites with thickness  $d_c$ ,  $K''(z)$  has a peak at  $z = d_c$  which refers to the distance between the two surfaces of the lamellae. Fig. 14 shows the temporal evolution

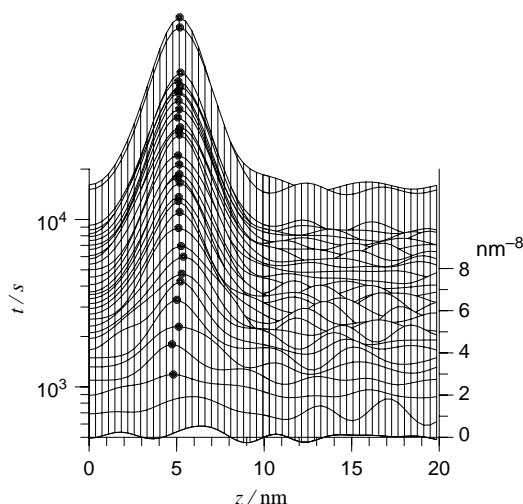


Fig. 14. PEO14, crystallization at 92 °C: Temporal evolution of the IDF. The times of the measurements follow from the starting points at the log  $t$ -axis on the left; the linear scale of the IDFs is plotted on the right side [23].

of the IDF derived from a time-dependent SAXS experiment on crystallization of PEO14 (from Ref. [23]). Results indicate formation of crystallites with an invariant thickness of 5 nm. The changing crystal thickness accompanying sequence length segregation would show up in a continuous peak shift.

Fig. 15 shows the same result—a time invariant crystal thickness—obtained for a commercial sPP that included steric defects (the sample had 83% syndiotactic pentads) [13].

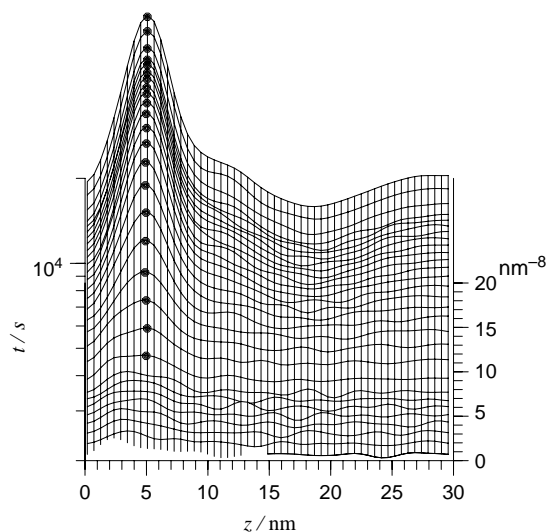


Fig. 15. sPP-Fina, crystallization at 108 °C: evolution of the IDF [13].

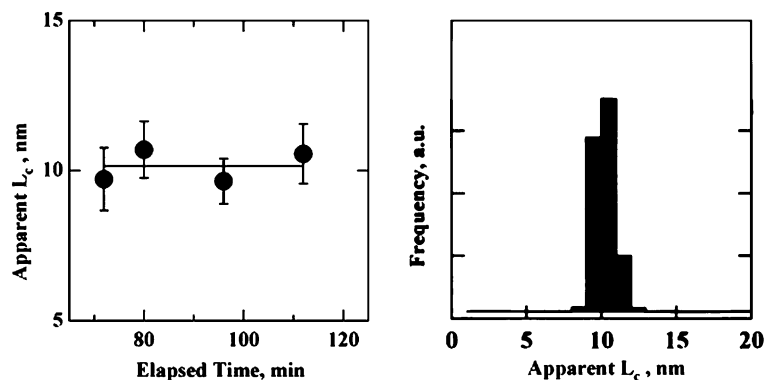


Fig. 16. PET, crystallization at 233 °C recorded by in situ AFM. Results of numerical image analysis: (left) time-dependence of the mean crystal thickness and (right) thickness distribution in the final state. Reproduced with permission from Ivanov et al. [25]. Copyright (2001) American Chemical Society.

In many discussions, crystal thickness variations are also assumed for crystallizing homopolymers, in the sense that the first grown dominant lamellae should be thicker than the later developed subsidiary crystallites. Bassett et al. had already opposed this view on the basis of TEM images, which show equal thicknesses for both, dominant and subsidiary crystallites [24]. Confirmation of the thickness uniformity now has come also from in situ AFM studies. Fig. 16 is taken from a work of Ivanov et al. [25]. It shows results of a numerical analysis of images obtained for PET during crystallization at 233 °C: The thickness distribution is rather sharp, and the mean thickness is constant throughout the whole crystallization process. A time-dependent SAXS study carried out at the same crystallization temperature for comparison yielded the same result.

#### 4.2. Polyethylene: crystal thickening

The majority of crystallization experiments have been carried out on high density polyethylene (HDPE) for obvious reasons: it is a major commercial product with high crystallinity, has a simple chemical structure, and is stable in heat treatments. However, HDPE has peculiar properties that introduce complications into crystallization experiments. Since sliding motions are active in the crystalline state, crystals thicken spontaneously, following a logarithmic law  $d_c = C_1 \log t + C_2$ . What is of interest in basic studies is the thickness of the lamellar crystallites when they form, but measurements always catch a later state modified by thickening. In basic studies, it is thus preferable to use branched or copolymerized PEs since the presence of the hetero-units blocks the sliding motion; they cannot be drawn into the crystal. Fig. 17 reproduces the results of a time-dependent SAXS experiment on a sample of HDPE [26].

The broad peak with a maximum at 21 nm is assigned to the crystallites. It moves with increasing time to higher  $d_c$ -values. The properties of the amorphous layers are also peculiar. The constant position of the IDF maximum at 10 nm indicates that their most probable thickness—which is near to the minimum value—remains constant throughout the crystallization process. The wide skewed distribution at the beginning narrows and converges towards the most probable value. Hence, in contrast to all the other polymers, where  $d_c$  is fixed, in HDPE it is the thickness of the amorphous layers, which has a characteristic fixed value. There are more polymer systems with longitudinal chain mobility in the crystalline state, which consequently also show spontaneous crystal thickening at the crystallization temperature. These include *i*-polypropylene, poly(ethylene oxide),

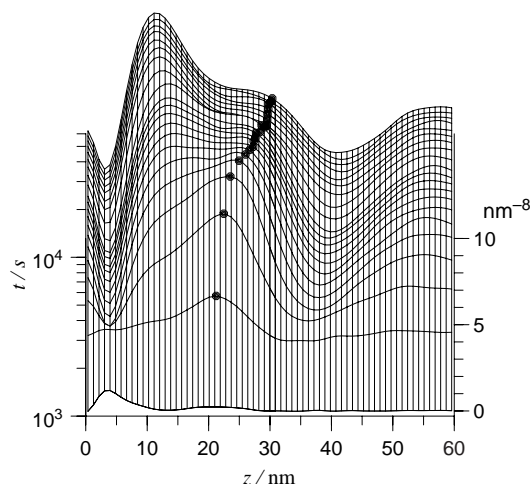


Fig. 17. HDPE: evolution of the IDF during crystallization at 129 °C. The shift of the maximum (filled circles) indicates continuous crystal thickening. The peak located at  $z \approx 10$  nm is associated with the amorphous layers in the stacks [26].

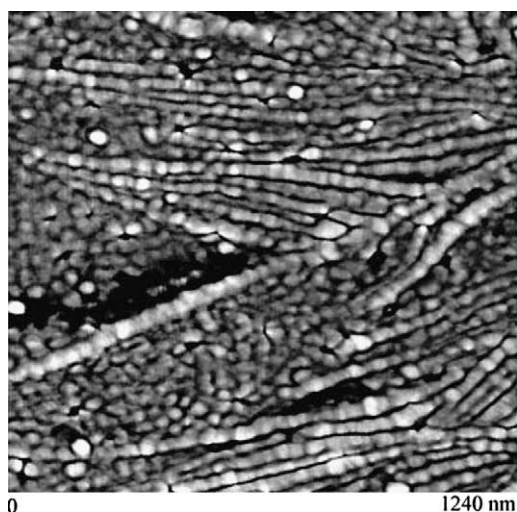


Fig. 18. sPP, crystallized at 135 °C: AFM tapping mode phase image. The edge-on oriented lamellae show a granular substructure [28,29].

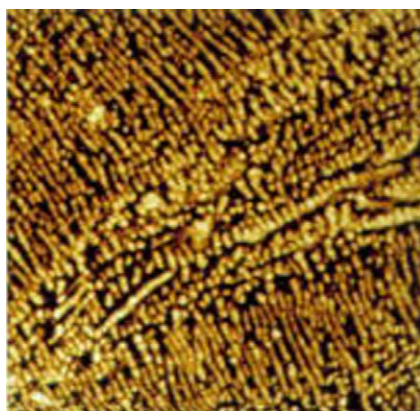
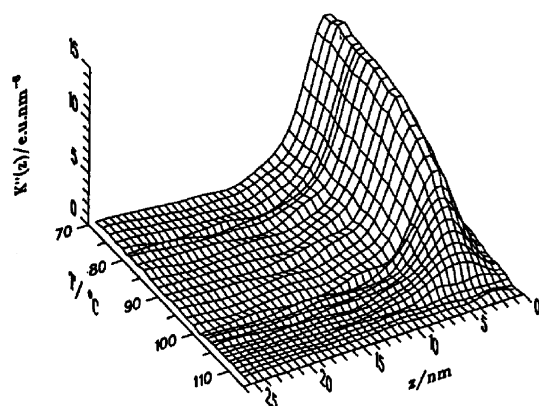


Fig. 19. iPP: AFM tapping mode phase image showing a granular substructure of the edge-on oriented crystal lamellae (1 μm scan). Reproduced with permission from Magonov et al. [30].



poly(oxyethylene), poly(vinylalcohol) and poly(tetrafluoroethylene), citing only the most common ones. An article by Schmidt-Rohr and Hu [27] collects the evidence from NMR spectra for the sliding motion and discusses the peculiar drawing properties—the ‘ultra-drawability’—of these systems.

## 5. Granular substructure of lamellae

It has long been known that lamellae formed when a polymer crystallizes have a granular substructure. Evidence is provided by the widths of the Bragg reflections in wide angle X-ray scattering (WAXS) patterns. For polymers they are much broader than for low molar mass crystals, and generally indicate lateral coherence lengths of several to some tens of nanometers. This is the same order of magnitude as the lamellar thickness. The block structure also shows up in TEM images when the staining agent penetrates into the block boundaries within the lamellae.

There are cases where the granular substructure becomes also apparent in AFM tapping-mode images, and two examples are presented here. That shown in Fig. 18 was obtained for sPP with high syndiotacticity [28,29]. A thin film of the sample was isothermally crystallized at 135 °C. The lamellae, oriented edge-on, show the granular substructure. Many images showing this property for various semicrystalline polymers were obtained by Magonov et al. [30,31]. Fig. 19 presents as one example the texture of a sample of isotactic polypropylene (iPP). Images of PE that show the blocky substructure were published by Loos et al. [32] and Goderis et al. [33]. In the latter work, block sizes in AFM images and coherence lengths derived from reflection

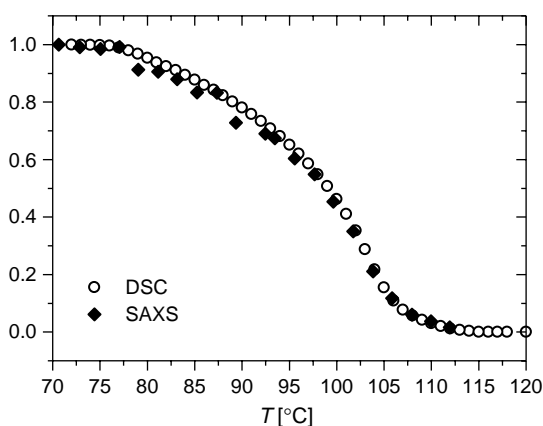


Fig. 20. sPPcO15, crystallized at 70 °C and heated to melting: (left) change of the interface distribution function  $K''(z)$ . (right) Continuous decrease of crystallinity,  $\phi_c(T)/\phi_c(70\text{ °C})$ , recorded by DSC and SAXS (heating rate: 1 K/min) [6].

halfwidths in WAXS patterns were compared. The agreement was satisfactory.

The blocky substructure is fundamental for the deformation properties of semicrystalline polymers [34,35]. A main yielding mechanism is block sliding, and this sets in cooperatively at the yield point. The strain-controlled, comparatively simple deformation properties of semicrystalline polymers are mainly based on the many degrees of freedom offered by

block sliding—internally stiff crystal layers would cause a quite different, much more complex deformation behavior.

## 6. Crystal stability variations

The uniformity in thickness of lamellar crystallites, which generally results if crystallization processes are conducted isothermally, does not imply uniform

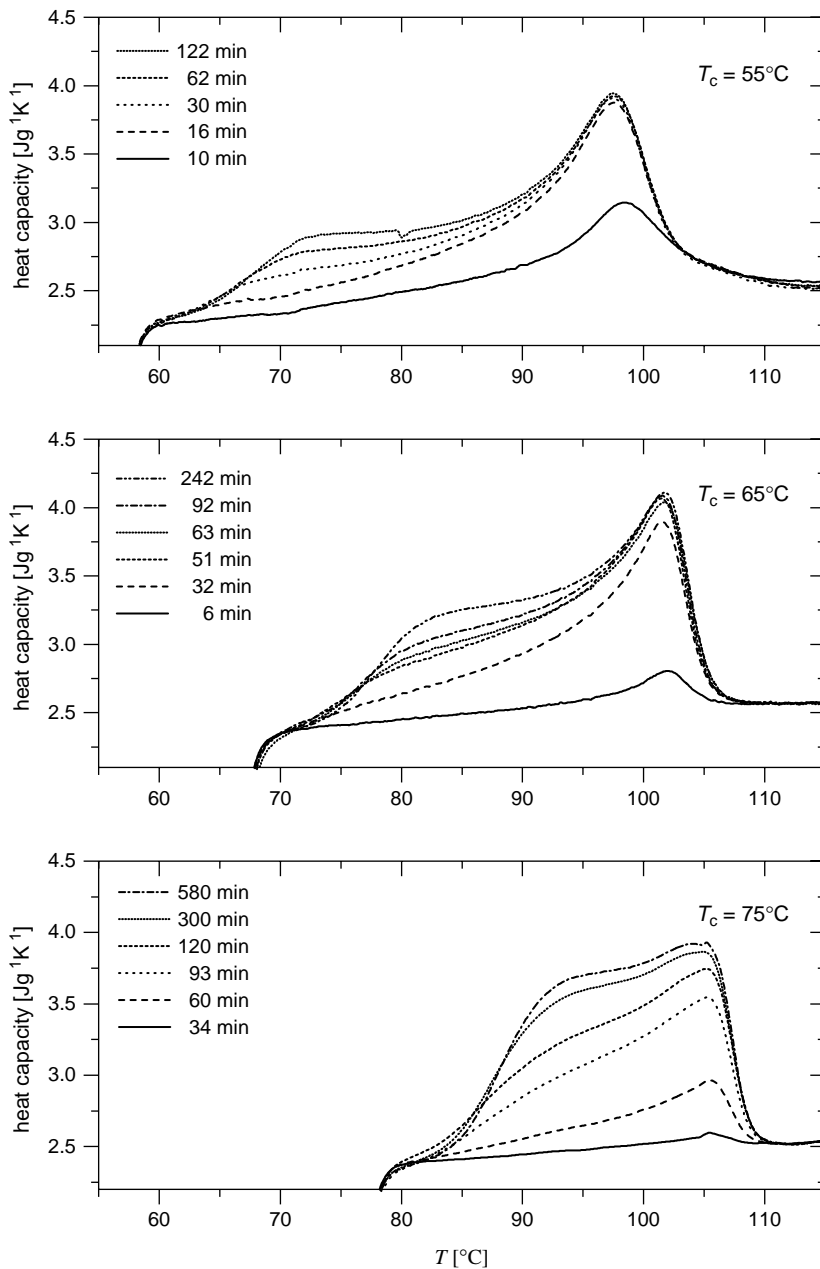


Fig. 21. sPPcO15: DSC-melting curves obtained after different times of isothermal crystallization at 55 °C (top), 65 °C (center) and 75 °C (bottom) [6].

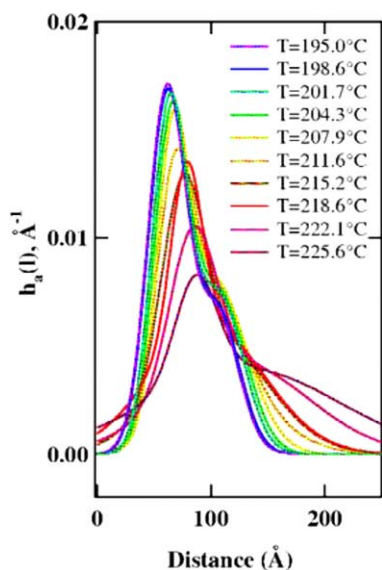


Fig. 22. PTT crystallized at 195 °C and then heated stepwise to the indicated temperatures. Results of a SAXS data evaluation: changes in the distribution function for the amorphous layer thickness,  $h_a(D)$ . Reproduced with permission from Ivanov et al. [37]. Copyright (2004) Springer-Verlag.

stability. In a subsequent heating process, melting still extends over a broad temperature range. Conventional views often associated melting point variations with a corresponding distribution of lamellar thickness only, but recent experiments now point to further sources of variations in crystal stability. In particular, some new experiments demonstrate, that the stability of crystals is not yet fixed when they are formed, but often improves with time.

### 6.1. Thermal response

Fig. 20 shows the melting behavior of a sample of poly(propylene-*co*-octene) with 15% by weight of octene co-units (sPPcO15) which was isothermally

crystallized at 70 °C (from Ref. [6]). The change in crystallinity during heating with a rate of 1 K/min was monitored by both the product  $Pd_c \propto \phi_c$  deduced from the SAXS curves and the enthalpy  $H$  derived from heat capacity measurements by DSC. The plot on the right shows in both measurements a continuous decrease of  $\phi_c$  with rising temperature. The plot on the left presents the change of the IDF during heating. The maximum of the peak is 3.7 nm for all temperatures; only the peak height decreases. Hence, the stabilities of the crystallites vary despite a common thickness—the first melt already at 75 °C, i.e. 5 °C above the crystallization temperature, the last disappear at 105 °C.

Part of the stability variations can be associated with the sequential building up of the spherulites. A TEM study of Bassett and Patel on poly(4-methylpentene-1) [36] has shown that the subsidiary lamellae always melt prior to the dominant crystallites even though both have the same thickness [24]. Fig. 21 presents analogous DSC observations for sPPcO15 (from Ref. [6]). The sample was isothermally crystallized at three values of  $T_c$ , for various times of crystallization. The structures developed during the preset times were probed by heating scans. It is evident that all the crystals first developed have high melting points, i.e. the highest possible stability, whereas the crystals formed later melt much earlier, i.e. are less stable.

Bassett and Patel related the lowering of the stability of subsidiary crystallites to constraints encountered during the in-filling process. Ivanov et al. quantified these constraints in a recent temperature-resolved SAXS study of the melting of isothermally crystallized poly(trimethylene terephthalate) (PTT) [37]. A model-based analysis yielded the thickness distribution function of the interlamellar amorphous layers. Fig. 22 presents this distribution function during heating. It is evident, that the thinnest amorphous layers disappear first, which indicates that crystals with the nearest neighbors have the lowest stability. Hence, the stability

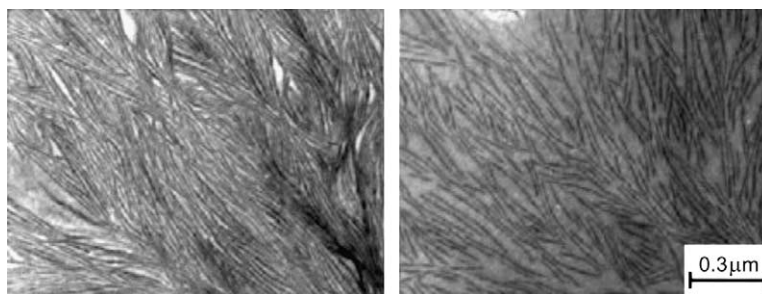


Fig. 23. iPS, cold-crystallized at 160 °C (left) and then annealed at 215 °C for 30 min (right): TEM micrographs obtained after quenching to room temperature. Reproduced with permission from Petermann et al. [38]. Copyright (2001) American Chemical Society.

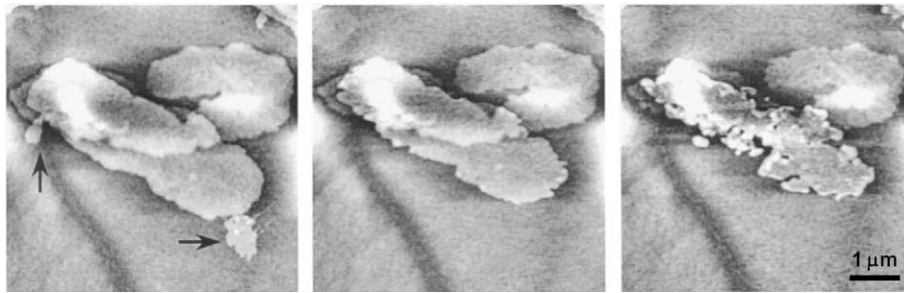


Fig. 24. Polyether BA-C8, crystallized at 75 °C (left), then annealed at 77 °C for 30 min (center) and at 79 °C for 10 min (right): AFM tapping-mode images of a flat-on oriented crystal. From Li et al. [39].

of a crystal depends not only on its inner structure and its surface, but also, for in-filled crystals, on the interaction between neighbors.

Microscopy observations have shown that besides the stability difference between dominant and subsidiary crystals there exist also stability variations within a single lamella. Two images obtained by Petermann et al. for *i*-polystyrene (iPS) in a TEM are reproduced in Fig. 23. The micrograph on the left shows the lamellar structure which developed in a thin film after crystallization at 160 °C; the picture on the right shows the changes caused by 30 min annealing at 215 °C. In both cases the sample was quenched to room temperature for observations. Many of the initial continuously extended lamellae become fragmented upon annealing.

Fig. 24 presents AFM images obtained by Li et al. for the polyether BA-C8 [39]. The lamellae appearing flat-on in the pictures grew during crystallization at 75 °C and were then annealed at 77 and 79 °C. The annealing initiated melting, but not in a homogeneous manner. Corrugations in the originally smooth lateral surfaces were produced and also holes in the interior. Hence, despite their initial uniform appearance, some parts of a lamella are more stable than others.

## 6.2. Stabilization during crystallization

Crystallites with the highest stability, i.e. those with the highest melting points, do not possess this stability from the very beginning. There exist several experiments which show a time dependence of the stability or an ordering within the crystalline state. We present here three selected studies:

- The stability of crystallites is probed by applying short temperature pulses during a dynamic mechanical experiment.
- Ordering processes associated with the crystallization are resolved by time-dependent IR spectroscopy.

- Changes in the internal structure of the crystallites show up in a time-dependent simultaneous small angle and wide angle X-ray scattering experiment.

Wurm and Schick devised a novel technique to test lamellae stability during an ongoing crystallization, and applied it to the crystallization of poly( $\epsilon$ -caprolactone) (P $\epsilon$ CL) [40]. The storage modulus  $G'$  was monitored as crystallization ensued at an annealing temperature of 331 K, and for a time subsequent to the imposition of a 4 K high temperature pulse, an insufficient increment to reach the melting temperature of the bulk sample. Six experiments were performed, with pulses applied after annealing times of 7000, 12,000, 17,000, 25,000, 40,000

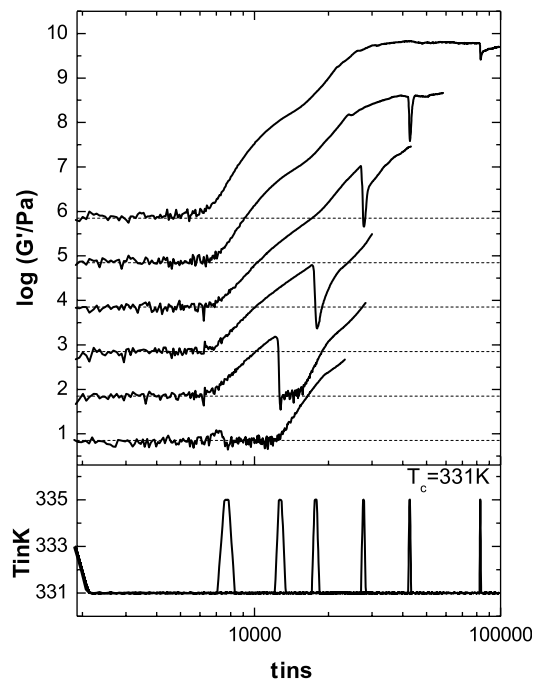


Fig. 25. P $\epsilon$ CL crystallized at 331 K: temporal development of the shear modulus  $G'$  when a temperature pulse of 4 K height is applied after various times. From Wurm et al. [40].

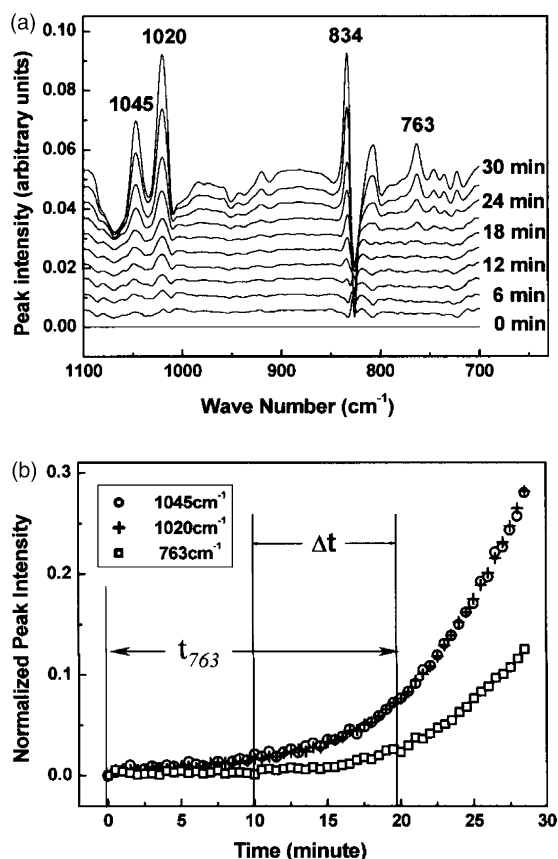


Fig. 26. Polyether BA-C10 crystallized at 65 °C: temporal variation of the IR difference spectrum (top). The bands at 1045, 1020 and 834  $\text{cm}^{-1}$  show up if the chain conformation is that of the crystalline state, the band at 763  $\text{cm}^{-1}$  requires, in addition, the lateral packing of the ordered unit cell. There is a time delay in the development of the bands (bottom). Reproduced with permission from Li et al. [41]. Copyright (2003) Elsevier Science Ltd.

and 80,000 s, as shown in Fig. 25. In all cases, the effects of crystallization began to appear in  $G'$  after about 6,000 s. In the first two cases (7000 and 12,000 s), the temperature pulse reduced  $G'$  to the value in the melt, with crystallites developing again on further annealing. This suggests that the pulse was sufficient to destroy the existing crystal lamellae thus showing that they had not reached their ultimate stability. By contrast, it may be seen that the drop in  $G'$  on more delayed pulses decreases with rising delay time, indicating that the stability of the crystallites increases with increasing annealing time.

Li et al. investigated the crystallization of the polyether BA-C10 by time-dependent IR spectroscopy [41]. The functional groups in the chain give characteristic peaks in the spectra, with clear variations between the crystalline and the amorphous state. Some of the bands show up only for the regular conformation associated with the crystalline state, and one of these bands requires in addition the regular lateral chain packing of the unit cell. Fig. 26 presents the temporal development of such bands, and the legend describes this general assignment. As can be seen, the three bands which are conformationally sensitive appear prior to the band which probes the regular packing (both intensities are normalized with regard to the final value). Hence, the experiments indicate a time delay between the transition of the chains into helical form and the intermolecular packing process.

A sensitive method of detecting small differences in the temporal development of bands in the infrared spectrum is provided by the 2D-correlation technique introduced by Noda [42,43]. Correlation functions are calculated for the time dependence of the intensity changes at two frequencies in different parts of the

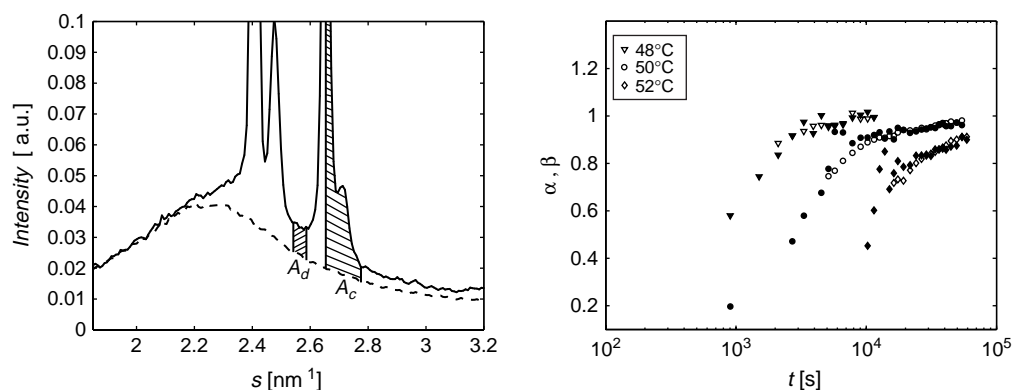


Fig. 27. PεCL, results of time-dependent SWAXS experiments. (left) WAXS pattern showing diffuse scattering from the crystals; the ratio  $\beta = A_c/A_d$  measures the intracrystalline order. (right) Time dependence of  $\beta$  (filled symbols) and of the SWAXS ratio  $\alpha = A_c/P$  (open symbols) choosing equal end values [46].

spectrum, and show whether or not there is a synchronous development. Recently, this tool was also applied to polymers that crystallize under different conditions [44,45]. One always finds time differences in the development of different bands, indicating a buildup of crystalline order in stages.

Intracrystalline disorder that decreases with time was also detected in a simultaneous small angle and wide angle X-ray scattering experiment (SWAXS) carried out on crystallizing P $\epsilon$ CL [46]. While SAXS is produced whenever lamellae exist that have a higher density than the melt, independently of their internal structure, the Bragg reflections in the WAXS originate only from crystal lattices only. Therefore, comparing the time dependences of the intensity of a Bragg reflection and the Porod coefficient  $P$  allows one to check whether the intralamellar state of order varies during the crystallization process. Fig. 27 shows on the right for various crystallization temperatures the time dependence of the ratio  $\alpha$  between the two parameters. It indeed increases with time. A look at the WAXS curve depicted on the left shows that the increase is due to an intracrystalline ordering process. The scattering curve initially obtained for the melt, adjusted to the curve obtained in the semi-crystalline state, is shown in the figure. The fit demonstrates that the crystallites produce a diffuse scattering, and this means that they are disordered. The base part of the reflections seems to be broadened which is indicative of spatially correlated perturbations. Two angular ranges were selected, one with diffuse scattering only and another including two Bragg reflections. The associated integrated intensities  $A_d$  and  $A_c$  were used to calculate the ratio  $\beta = A_c/A_d$ , which serves as a measure for the degree of order within the crystals;  $\beta$  is also shown in the right hand figure, and it changes with time in a similar manner as  $\alpha$ . Hence, both time dependences indicate that crystals

are perturbed in the initial stage of formation and then gradually improve their order.

## 7. Crystallization line and melting line

Considerations about mechanisms of crystallization and melting in polymers require as a basic ingredient knowledge of:

- the variation of the crystal thickness  $d_c$  with the crystallization temperature  $T_c$  and
- the variation of the final melting temperature  $T_f$  with crystal thickness.

Time and temperature-dependent SAXS experiments make it possible to determine these relationships and have been carried out for several polymer systems. Investigations were facilitated by the invariance of the crystal thickness during the crystallization process. Some of the measurements have already been presented. The IDFs for PEcO14 in Fig. 14 yielded the thickness resulting from crystallization at 92 °C; Fig. 20 showed for a sample of poly(propylene-*co*-octene) a series of IDFs obtained during heating, from which the melting point  $T_f$ —here 103 °C—was derived.

### 7.1. $T_c$ - $d_c$ - $T_f$ relationships

SAXS experiments have been reported for syndiotactic polypropylene and copolymers [6], poly(ethylene-*co*-octene)s [26,47], isotactic polypropylene [48], isotactic polystyrene [49], poly(1-butene) [50] and poly( $\epsilon$ -caprolactone) [47]. Figs. 28–30 show three selected examples of the results obtained: for an octene copolymer of sPP (15% by weight of octene units), an octene copolymer of PE (14% by weight of octene units) and P $\epsilon$ CL. The Gibbs–Thomson equation describes the melting point  $T_f$  of a crystallite with thickness  $d_c$  (heat

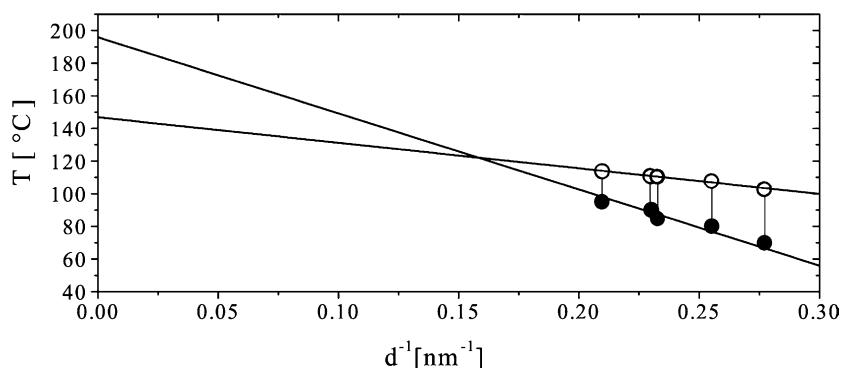


Fig. 28. sPPcO15: crystallization line  $T_c$  versus  $d_c^{-1}$  (filled symbols) and melting line  $T_f$  versus  $d_c^{-1}$  (open symbols) [6].

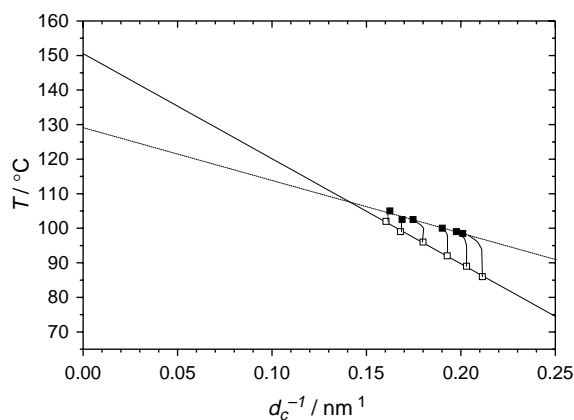


Fig. 29. PEcO14: crystallization line and melting line. The connecting lines show the temperature dependence of  $d_c^{-1}$  during heating [47].

of fusion  $\Delta h_f$ , surface free energy  $\sigma_{ac}$ ) as

$$T_f(d_c) = T_f^\infty - \frac{2\sigma_{ac}T_f^\infty}{\Delta h_f d_c} \quad (8)$$

This equation suggests plotting the melting points as a function of the inverse crystal thickness  $d_c^{-1}$ , and the same representation was then also used for the relation between  $T_c$  and  $d_c$ .

The appearance of the plots is typical of all the samples investigated: two straight lines that cross. The ‘melting line’ giving the relation between  $T_f$  and  $d_c^{-1}$  confirms the Gibbs–Thomson equation. This allows a determination of the equilibrium melting point  $T_f^\infty$  by a linear extrapolation to  $d_c^{-1} = 0$ . The novel feature in the results is the ‘crystallization line’ giving the relation between  $T_c$  and  $d_c^{-1}$ . It has a greater slope than the melting line, intersects the latter at a finite value of  $d_c^{-1}$  and approaches a limiting temperature as  $d_c^{-1} \rightarrow 0$ ,

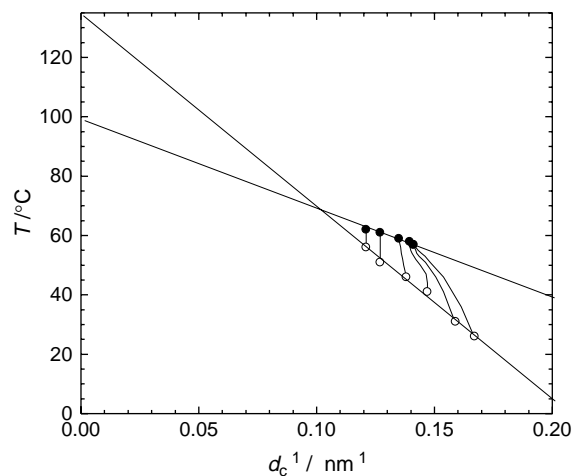


Fig. 30. PeCL: crystallization line and melting line [47].

denoted  $T_c^\infty$ , which differs from  $T_f^\infty$ . The crossing implies that  $T_c^\infty$  is always greater than  $T_f^\infty$ . The results of the temperature dependence measurements during heating are given by the thin lines in Figs. 28–30, which connect respective points on the crystallization and the melting line. The lines are vertical when the thickness remains constant and are curved when the crystal thickness increases during heating.

These results lead us to some conclusions that are—we believe—unambiguous. The existence of straight crystallization lines in all the systems investigated expresses a simple law: crystal thicknesses are inversely proportional to the distance from a certain characteristic temperature,  $T_c^\infty$ , and not, as conventional wisdom assumes, inversely proportional to the supercooling below  $T_f^\infty$ . In the examples given here,  $T_c^\infty$  is 20 to 50 °C above  $T_f^\infty$ . A second straightforward conclusion concerns the popular Hoffman–Weeks plot. Many authors derived equilibrium melting points of crystallizing polymers from DSC studies, plotting the temperature difference  $T_f - T_c$  against  $T_c$  and identifying the equilibrium melting point with that crystallization temperature where the temperature difference would vanish. The results in the figures demonstrate that this procedure is wrong. It yields the temperature of the intersection point between the melting and the crystallization line rather than  $T_f^\infty$ . Errors resulting from this incorrect assignment can be drastic. For example, for the PeCL sample the true equilibrium melting point, determined by extrapolation of the melting line to  $d_c^{-1} = 0$ , is located around 100 °C, whereas the Hoffman–Weeks plot yields a value of about 70 °C. It is the latter, wrong value which is given in the literature.

These conclusions are obvious; but what is the physical basis of the findings? The melting line describes the thickness dependence of a phase transition from the crystalline to the liquid state. Wouldn’t it be natural to interpret the crystallization line in an analogous way, i.e. again as the thickness dependence of a structural transition, but since  $T_c^\infty \neq T_f^\infty$ , certainly not another one between the crystalline and the fluid state? We have suggested such an understanding and below, in Section 9, we briefly explain our view.

Lamellar crystallites principally exist only at temperatures below the melting line. Therefore, crystals with thicknesses given by the crystallization line can no longer be formed when the temperature of the intersection point is approached. This has indeed been confirmed by an experiment [29,51]. SAXS results in the interesting temperature range were obtained for sPPcO20, and are shown in Fig. 31. The points deviate from the crystallization line before reaching

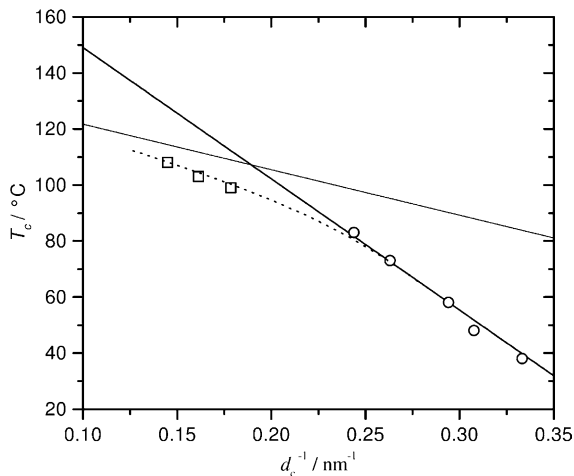


Fig. 31. sPPcO20: relation between crystallization temperature and crystal thickness near the point of intersection between the melting- and the crystallization line. Isothermal crystallizations were carried out with the aid of the self-seeding technique [29,51].

the intersection. In this experiment, crystallization was conducted using the self-seeding procedure, i.e. the sample was quickly heated above its melting point and then crystallized again. As was also mentioned in Section 3.2, memory effects then reduce the crystallization time. For crystallization studies in this range, there is no other way to achieve crystal formation. On cooling an equilibrated melt to temperatures near the intersection point, crystallization times become unacceptably long.

### 7.2. Effects of co-units, diluents, blending and molar mass

The presence in a chain of co-units or stereo defects that cannot be included in the crystal lattice, and of low molar mass diluents or a second, but noncrystallizable, polymer in the melt modifies the crystallization and melting properties. Variations are also to be expected with the molar mass of a sample. SAXS and WAXS time and temperature dependent investigations carried out to observe these effects led to some unexpected results.

The findings for sPP and a variety of related octene-copolymers [6], depicted in Fig. 32, came as a complete surprise: in contrast to the normal behavior of the melting lines, which shift to lower temperatures when the co-unit content increases, the crystallization line is invariant within this set of samples. One observes a unique  $T_c$  versus  $d_c^{-1}$  relation common to all of them, which determines  $d_c$  as being inversely proportional to the supercooling below  $T_c^\infty = 195$  °C.

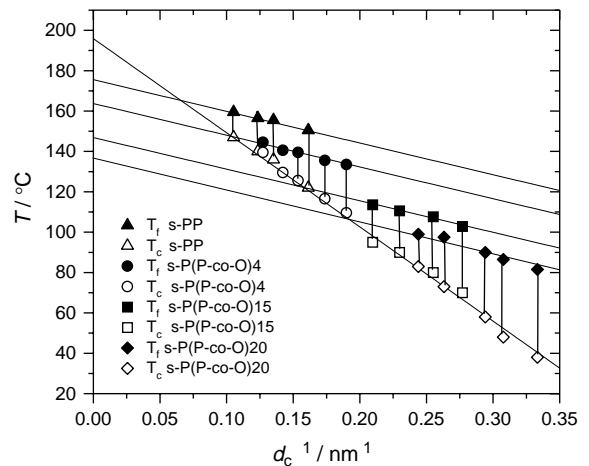


Fig. 32. sPP and sPPcOx (x% octene co-units by weight): unique crystallization line (open symbols) and series of melting lines (filled symbols) [6].

The same invariance is also found for the lateral size of the blocks in the lamellar crystals [52]. Crystal block diameters can generally be derived from the linewidth of Bragg-reflections in WAXS patterns, by application of the Scherrer equation

$$D_{hkl} = (\Delta s_{hkl})^{-1} \quad \text{with } s = 2(\sin \theta)/\lambda \quad (9)$$

where  $\Delta s_{hkl}$  denotes the integral linewidth of the  $hkl$ -reflection. Fig. 33 presents the diameter thus obtained for a set of different sPPs, with a sample of high syndiotacticity (sPP), a commercial sample with lower tacticity (Fina sPP), and two octene copolymers. The given lengths were derived from the linewidth of the 200-reflection, i.e. they refer to the direction perpendicular to the 200 lattice planes. As can be seen, all

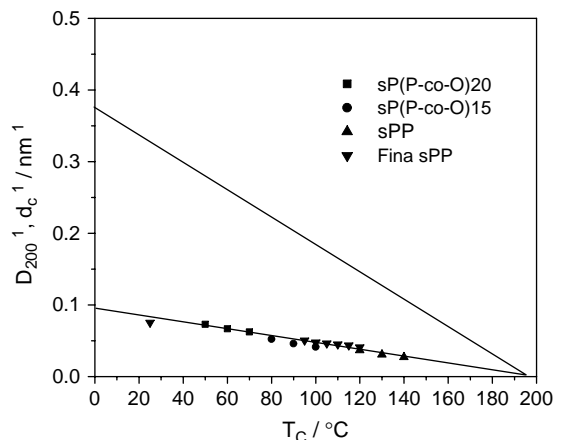


Fig. 33. Samples of sPP and sPPcOx crystallized at various  $T_c$ 's: lateral block lengths  $D_{200}$  derived from the linewidth of the 200-reflection (filled symbols) and crystallization line from Fig. 32 [52].

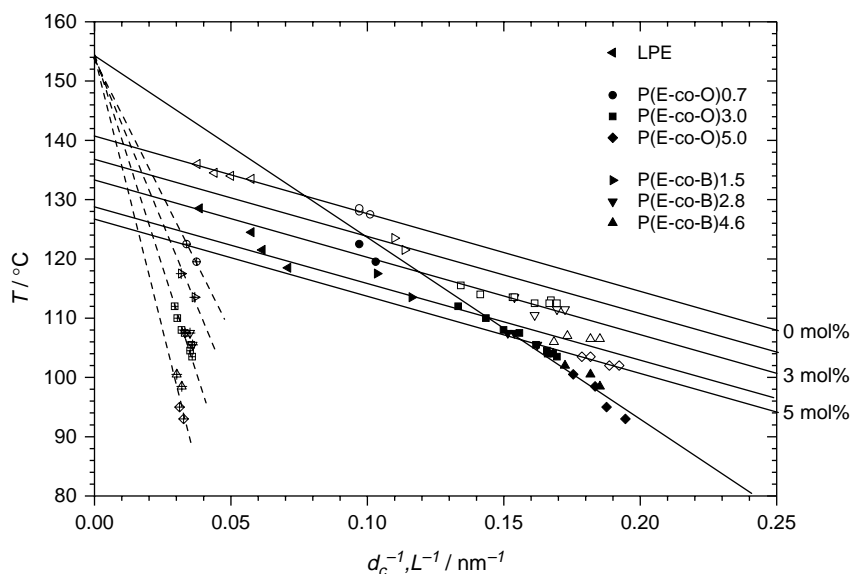


Fig. 34. Samples PEc(B/O)x (x: mol% butene or octene units): crystallization line (filled symbols) and melting lines (open symbols). The dotted lines give long spacings measured after completion of the crystallization process [26].

points  $D_{200}^{-1}(T_c)$  fall on a common line. When continued, this line ends at  $T_c^{\infty} = 195$  °C, like the crystallization line of sPP (which is also included in the figure).

Analogous results were obtained for PE and copolymers with butene and octene units; they are reproduced in Fig. 34 (from Ref. [26]) and Fig. 35 (from Ref. [52]). On increasing the co-unit content, the expected downward shift of the melting lines is found, but again a crystallization line that is common for all copolymers. Strictly speaking, this is valid for all samples with more than 1.5 mol% of co-units. For the samples with less co-units deviations occur, for the same reason—lamellar thickening—as in the case of HDPE (see Section 4.2), which is also included in the figure. Extrapolation of the crystallization line yields  $T_c^{\infty} \approx 154$  °C. Interestingly, the same limiting temperature was found for the temperature dependence of the long spacing, given by  $L \propto 1/(T_c^{\infty} - T_c)$ . Fig. 35 shows the temperature dependence of the block length perpendicular to the 110 lattice planes for three poly(ethylene-co-octene)s. There is one common dependence, described by  $D_{110} \propto 1/(T_c^{\infty} - T_c)$ .

Fig. 36 presents a third system with such findings. Using SAXS, Ree et al. determined the thicknesses of crystallites and amorphous layers in poly(ethylene terephthalate) (PET) and two related isophthalate-copolymers (PETcIT)) [53]. Crystal thicknesses depend on the crystallization temperature only, whereas

the amorphous layer thickness increases with rising co-unit content.

In order to see the effect of diluents on the crystallization and melting behavior SAXS experiments were carried out for mixtures of PEcO14 with two diluents, namely *n*-hexadecane ( $C_{16}H_{34}$ ) and methylanthracene ( $C_{15}H_{12}$ ) [23]. Results reproduced in Fig. 37 show the following:

- The two diluents equally suppress the melting points. The shift of the melting line increases linearly with the mole fraction of co-units  $x$ , in agreement with

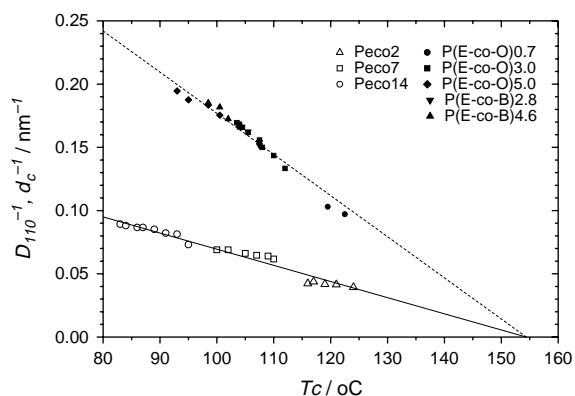


Fig. 35. Samples PEcOx (x: weight% octene units) crystallized at various  $T_c$ s: lateral block sizes  $D_{110}$  derived from the linewidth of the 110-reflection and crystallization line from Fig. 34 [52].

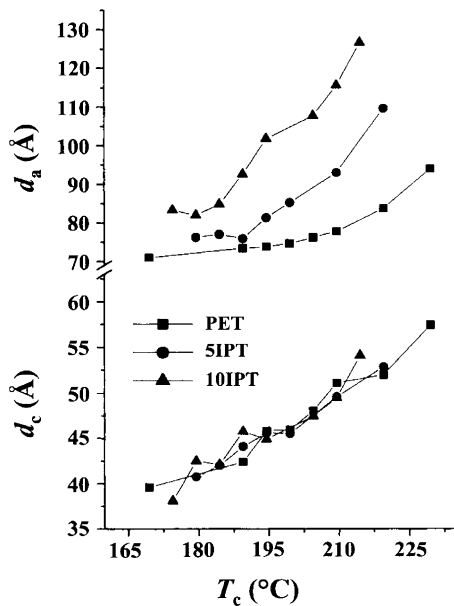


Fig. 36. PET and P(ETcIT): unique temperature dependent crystal thickness  $d_c(T_c)$  and changing amorphous layer thickness  $d_a(T_c)$ . Reproduced with permission from Ree et al. [53]. Copyright Elsevier Science Ltd.

Raoult's law:

$$T_f^\infty(x) = T_f^\infty - \frac{R(T_f^\infty)^2}{\Delta h_f} x \quad (10)$$

- The presence of  $C_{15}H_{12}$  leaves the crystallization line unaffected, unlike  $C_{16}H_{34}$ , which results in shifts even larger than those of the melting lines.

Groeninckx et al. investigated the effect of adding a non-crystallizable polymer to the melt, in a SAXS study of a mixture of polyethyleneoxide (PEO) with the amorphous polyamide Aramide34I [54]. Results for crystallization at 44 °C are given in Fig. 38. As is noted, the crystal thickness remains virtually unaffected, but the long spacing and the amorphous layer thickness increase.

The effect of the molar mass on the semicrystalline structure developing under isothermal crystallization conditions was investigated by Dosière et al. for a series of fractions of poly(ether-etherketone) (PEEK) [55]. The results are shown in Fig. 39; an increase in molar mass leads to thickening of the amorphous layer, but the crystal thickness  $d_c$  remains constant, depending only on the crystallization temperature.

Surveying all the observations, we see a most remarkable constancy of the crystal layer thickness at a given crystallization temperature, the only exception being the effect arising from addition of  $C_{16}H_{34}$  to PE.

We understand these findings as evidence for an interference of a third, mesomorphic phase along the crystallization pathway. Indeed, if co-units or diluents are already rejected when the mesomorphic phase forms, they have no influence on the crystal formation.

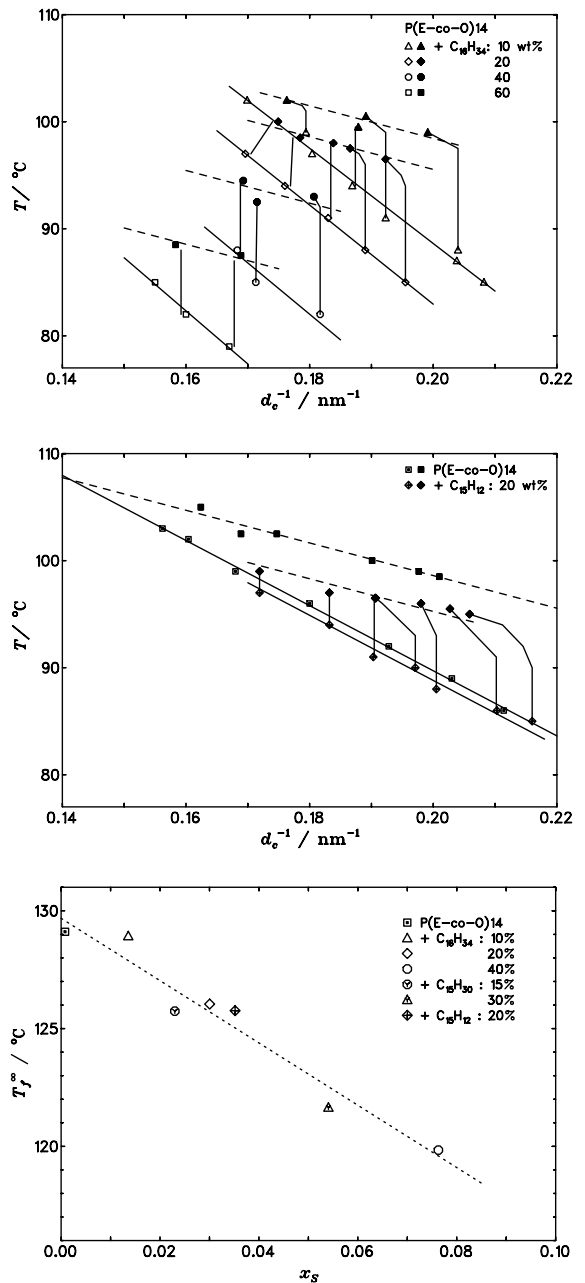


Fig. 37. (top) Polymer-diluent mixtures PEcO14/ $C_{16}H_{34}$  (90/10, 20/80, 40/60, 40/60): crystallization and melting lines. (center) Mixtures PEcO14/ $C_{15}H_{12}$  (100/0, 80/20): crystallization and melting lines. (bottom) Equilibrium melting points  $T_f^\infty$  determined by linear extrapolations of the respective melting lines: dependence on mole fraction of diluent [23].

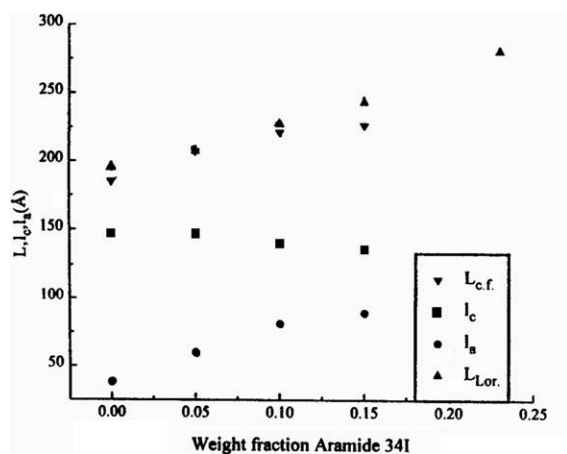


Fig. 38. PEO mixed with Aramide34I, crystallized at 44 °C: variation of crystal thickness  $l_c$ , amorphous layer thickness  $l_a$  and long spacing  $L$  with aramide content. Reproduced with permission from Groeninckx et al. [54]. Copyright (1999) Elsevier Science Ltd.

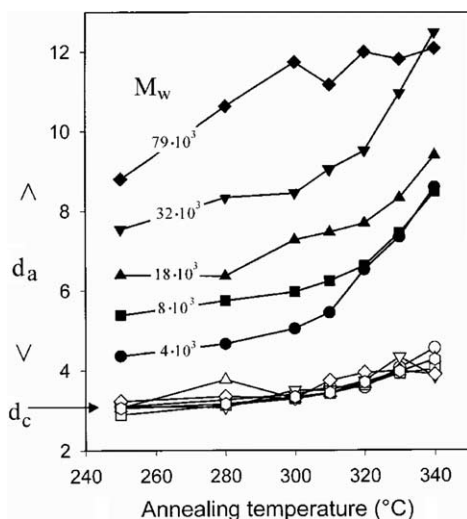


Fig. 39. PEEK fractions: temperature dependence of thicknesses of crystallites and amorphous intercrystalline layers for various molar masses. Reproduced with permission from Dosière et al. [55]. Copyright (1998) American Chemical Society.

## 8. Recrystallization processes

Heating an isothermally crystallized polymer is not always accompanied just by melting of the crystallites according to their stability. In many cases, the melting is immediately followed by formation of a new crystal. These ‘recrystallization processes’ can have different characteristics, depending on the crystallization temperature. Investigations applying temperature dependent

SAXS and DSC, and here in particular, the use of chip calorimeters at ultrahigh heating rates have provided new insights.

The results obtained are easy to interpret when samples have been crystallized at high temperatures. Fig. 40, taken from Ref. [56], presents as a typical example the behavior of an sPP sample with high tacticity (91% of syndiotactic pentads) during heating scans after crystallization at 115 °C. The IDF's derived from measured SAXS curves indicate a continuous slow decrease of crystallinity without crystal thickness changes, and a final melting at 145 °C. Subsequently, new crystallites form, with a steplike increased thickness corresponding to the temperature of their formation. On further heating, to 153 °C, these crystallites melt. The DSC scans presented on the right show this melting-recrystallization-melting process, and indicate that it occurs only if sufficient time is provided; for the higher heating rates this was not the case.

Fig. 41 presents as a second example SAXS and DSC results for an sPP sample with lower tacticity [57,58]. The vertical connecting lines between the points of crystallization (open circle) and melting (filled circles) at the highest  $T_c$  values exhibit the same properties as in the first case—melting possibly followed by recrystallization—however, for a crystallization at 25 °C, from the glassy state, a completely different behavior is found. The crystal thickness increases immediately when the heating begins, and the reorganization progresses steadily, continuing up to complete melting at 130 °C. The final melting also shows up in the DSC thermograms shown on the right. The ongoing reorganization gives no signal in the thermogram, which means that it proceeds at practically constant crystallinity. Only at the onset of recrystallization, just above  $T_c$ , does a weak signal appear. Shifting to lower temperatures on decreasing the heating rate is indicative of the nature of this low temperature endotherm: it reflects a competition between crystal disaggregation and reformation processes (and not, as is sometimes assumed, the melting of a small fraction of thin crystals). Properties intermediate between the two limiting cases following for  $T_c=120$  and 25 °C are found for  $T_c=100$  °C. Here, crystals are at first stable, i.e. keep their thickness constant, but when a certain limiting temperature is reached reorganization processes set in. The final melting point is again 130 °C, as for  $T_c=25$  °C.

Fig. 42 reproduces SAXS and DSC results that show the same scenario for iPS [58,59]. Samples crystallized at temperatures below 220 °C all experience a continuous recrystallization during heating, and melt

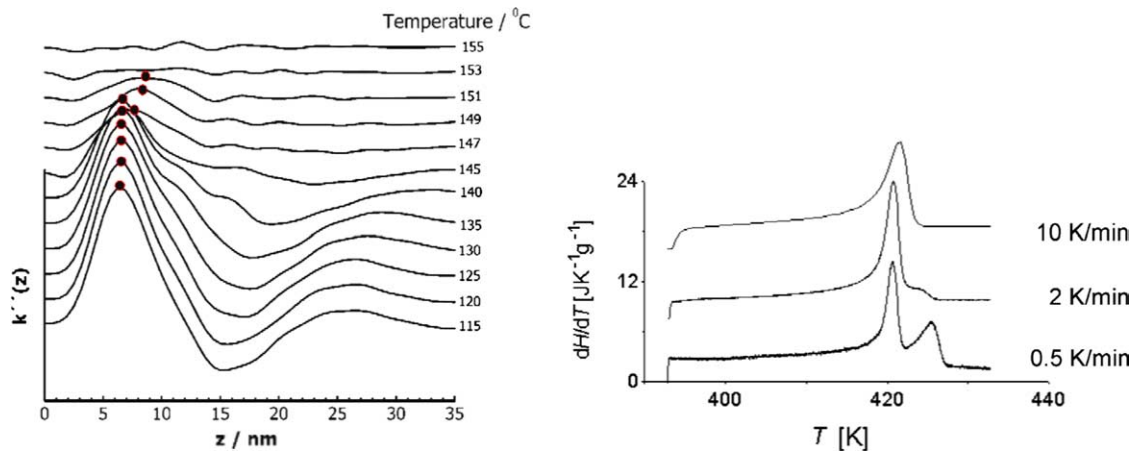


Fig. 40. sPP crystallized at 115 °C: (left) variation of the interface distribution function during heating to melting [56]; (right) DSC curves measured at three heating rates after crystallization.

at a constant temperature of 230 °C. Then, for  $T_c > 220$  °C, the melting temperature begins to vary, shifting to higher values with increasing  $T_c$ .

The structural reorganization setting in immediately for low  $T_c$ s is an extremely rapid process, much faster than the recrystallization process of Fig. 40 where the initial crystallization was conducted at a high  $T_c$ . Whereas the latter no longer occurs with a heating rate of 10 K min<sup>-1</sup>, suppression of the first requires heating rates four orders of magnitude higher. Schick et al. [60] studied the melting of cold-crystallized PET ( $T_c = 130$  °C) with a chip calorimeter, which allows for thin film heating rates up to 10<sup>5</sup> K min<sup>-1</sup>. Fig. 43 (on the left) reproduces some results. The thermograms measured for standard heating

rates resemble those in Fig. 41, showing a weak low temperature endotherm near  $T_c$  and one main melting endotherm. Increasing the heating rate leads at first to an increase of the amplitude of the low temperature endotherm and finally to a coalescence of the two signals. The coalescence is indicative of a transfer into the melt without prior reorganization, but the suppression requires a scanning rate of  $1.6 \times 10^5$  K min<sup>-1</sup>. The figure on the right explains how the low temperature endotherm in the standard scan could arise, namely, as was already mentioned in the discussion of the sPP data, by a superposition of melting and recrystallization processes. The superposition leads to a small exothermic net heat flow along the flat portion of the DSC curve. Here again,

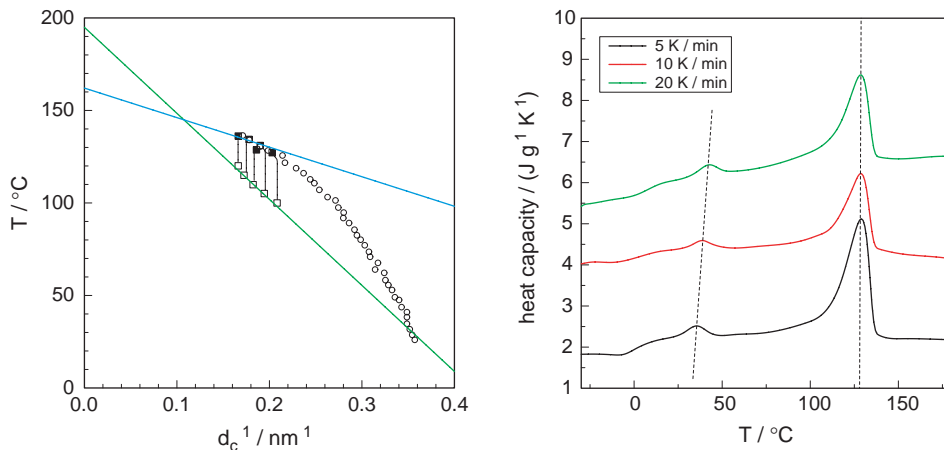


Fig. 41. sPP-Mitsui, quenched to the glassy state and then crystallized at 25 °C and at other temperatures in the range 100–120 °C. (left) Variation of crystal thickness during subsequent heating. Crystallization line from Fig. 32 and melting line. (right) DSC curves measured at three heating rates [57,58].

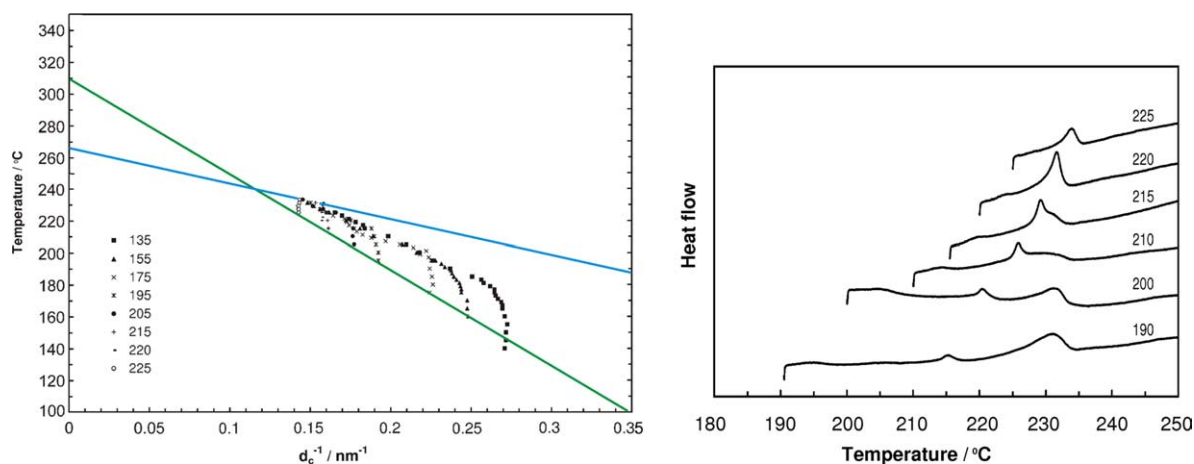


Fig. 42. iPS quenched to the glassy state and then crystallized at various temperatures. (left) Variation of  $d_c^{-1}$  during subsequent heating, obtained by SAXS experiments. Crystallization line and melting line. (right) DSC thermograms of samples, measured after isothermal crystallization processes with a heating rate of  $0.5 \text{ K min}^{-1}$  [58,59].

the only weak heat flow in the intermediate range between the low temperature and high temperature endotherms does not imply that the structure would remain constant. On the contrary, the structure varies throughout this range, but this is not accompanied by detectable crystallinity changes.

In conclusion, two different scenarios for the structural reorganization during heating scans subsequent to isothermal crystallizations are found:

- a low  $T_c$  pathway associated with continuous crystal thickening up to a fixed melting point, and
- a high  $T_c$  pathway with a constant crystal thickness and a melting point that rises together with  $T_c$ .

For the fast reorganization, there are good reasons to invoke passage through a mesomorphic phase rather than the melt. They are presented in Section 9.

## 9. Crystal thickness selection and melting properties

The above sections reviewed recent progress in the state of knowledge on two primary issues:

How does the thickness of the lamellar polymer crystallites,  $d_c$ , vary with

- the crystallization temperature  $T_c$
- the length distribution of crystallizable sequences, determined by the distribution of co-units or stereo

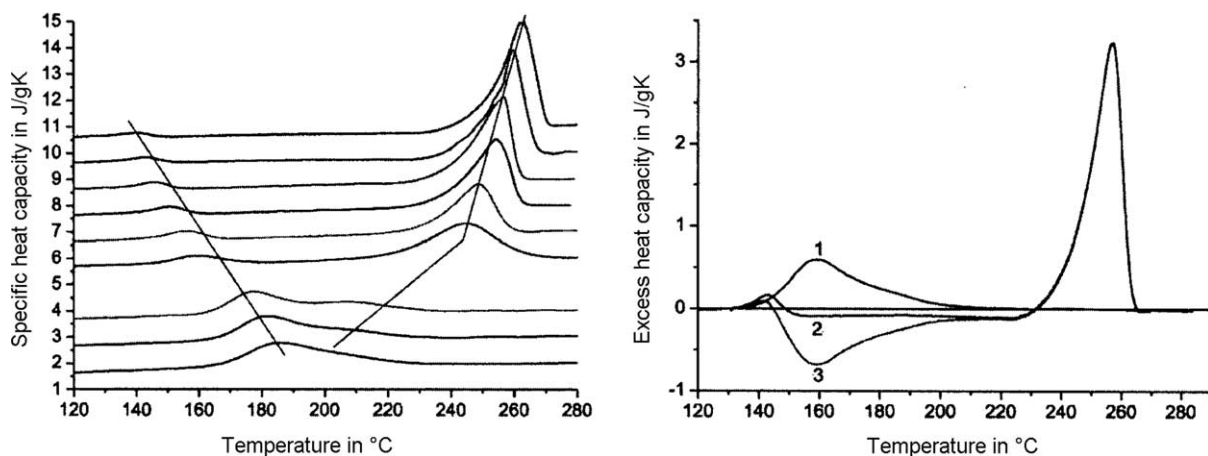


Fig. 43. PET, cold-crystallized from the glassy state at  $130 \text{ °C}$ : (left) DSC curves measured with different heating rates between  $2 \text{ K min}^{-1}$  and  $1.62 \times 10^5 \text{ K min}^{-1}$  using a high speed calorimeter. (right) Decomposition of the curve obtained with the lowest heating rate (2) into the contributions of melting (1) and recrystallization (3). Reproduced with permission from Schick et al. [60]. Copyright (2004) Elsevier Science Ltd.

defects

- the molar mass distribution?

How stable are these crystallites, i.e. how much can the temperature be raised without inducing structural changes?

The answer to the first question turns out to be surprisingly simple:  $d_c$  is uniform within a sample and varies inversely with the difference between  $T_c$  and a characteristic temperature  $T_c^\infty$  located above the equilibrium melting point  $T_f^\infty$

$$d_c \propto 1/(T_c^\infty - T_c) \quad (11)$$

$d_c$  is not at all affected by the distribution of crystallizable sequences and the molar mass. The answer to the second question is: the stability varies, in spite of the uniformity of  $d_c$ . The crystals with the highest stability maintain their structure up to a melting point given by the Gibbs–Thomson equation

$$T_f = T_f^\infty - Cl/d_c \quad (12)$$

For the crystals with the lowest stability, structural changes set in shortly above  $T_c$ . A new model associated with a thermodynamic scheme deals with these issues and describes the observations correctly [58]. It is presented in this section in shortened form, together with examples of applications.

### 9.1. Ostwald's rule applied to polymer crystallization

Early in the 1990s, Keller and his co-workers, Goldbeck-Wood, Hikosaka and Rastogi, carried out crystallization experiments on polyethylene at elevated pressures using a polarizing optical microscope [61]. They observed crystal formation via the hexagonal phase. Crystals nucleate into the hexagonal phase, then grow to sizes in the micrometer range before they transform into the orthorhombic phase after

a statistically initiated, second nucleation step. The authors interpreted their observations as a new example of Ostwald's rule of stages [3]. This rule, formulated about 100 years earlier, states that crystals always nucleate into that mesomorphic or crystalline structure which is the most stable one for nanometer-sized crystals. Because of differences in the surface free energy, this state may differ from the crystal modification which is macroscopically stable.

Searching for an understanding of polymer crystallization at normal pressures, we thought that Ostwald's rule of stages might again provide the clue. The observed controlling temperature for  $d_c$ , which is  $T_c^\infty$ , and not  $T_f^\infty$ , indeed indicates the interference of a transient mesomorphic phase. Unlike the statistically induced mesomorphic–crystalline transformation process observed for PE at elevated pressures, crystal thicknesses are now sharply selected. In a first attempt, a qualitative model was set up; Fig. 44 displays a sketch of it [51]. It is meant to describe different stages of growth of a lamellar crystallite. The process starts with an attachment of chain sequences from the melt onto a growth face of a mesomorphic layer of minimum thickness, which then spontaneously thickens. When a critical thickness is reached, the layer solidifies immediately by the formation of block-like crystallites. The last, but equally important step in crystal development is the stabilization of the crystallites in time, leading to a further decrease in the Gibbs free energy. In the sketch, this last step is represented as a merging of the blocks, but this is only one possibility.

The basic thermodynamic conditions under which a mesomorphic phase can interfere and thus affect the crystallization process are described in the drawing in Fig. 45.

This schematic plot shows for both the crystalline phase (c) and the mesomorphic phase (m) the difference of its bulk chemical potential to that of the melt (a)

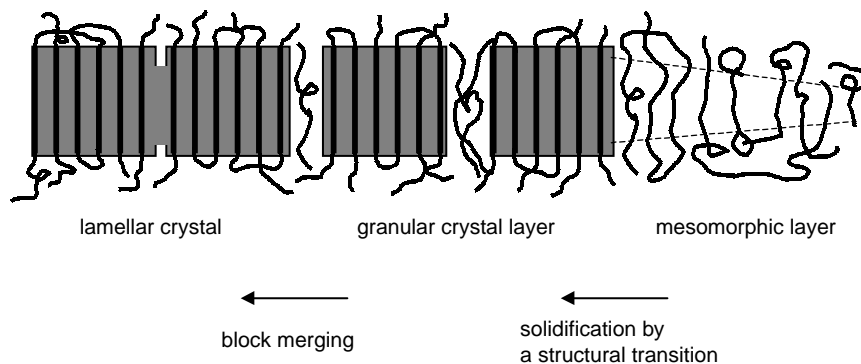


Fig. 44. Sketch of the pathway followed in the growth of polymer crystallites as suggested in Ref. [51].

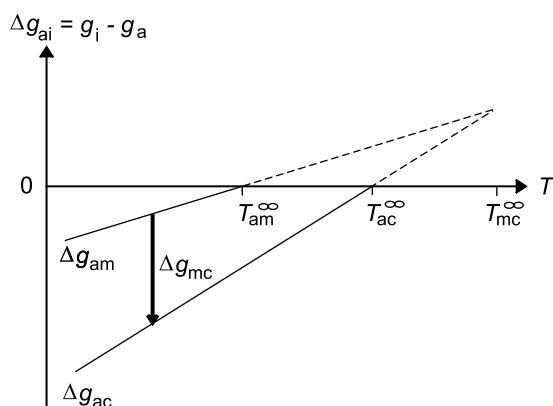


Fig. 45. Thermodynamic conditions assumed for crystallizing polymers: temperature dependences of the bulk chemical potentials of a mesomorphic and crystalline phase. The potentials are referred to the chemical potential of the melt and denoted  $\Delta g_{am}$  and  $\Delta g_{ac}$ , respectively [58].

$$\Delta g_{ac} = g_c - g_a, \quad \Delta g_{am} = g_m - g_a \quad (13)$$

Coming from high temperatures the chemical potential of the crystalline phase drops below the value of the melt when crossing the equilibrium melting point  $T_{ac}^{\infty}$ . The mesomorphic phase requires a lower temperature to bring its chemical potential below that of the melt, here at  $T_{am}^{\infty}$ . The plot includes also a temperature  $T_{mc}^{\infty}$ , which represents the temperature of a virtual transition, namely that between the mesomorphic and the crystalline phase. The transition temperatures fall the order  $T_{mc}^{\infty} > T_{ac}^{\infty} > T_{am}^{\infty}$ . Since the bulk chemical potential of the crystal is always below that of the mesomorphic phase, the latter is only metastable for macroscopic systems. However, for small objects, with sizes in the nanometer range, stabilities can be inverted. Due to a usually lower surface free energy, thin mesomorphic layers can have a lower Gibbs free energy than a crystallite of the same thickness. Then Ostwald's rule of stages applies.

## 9.2. A thermodynamic multiphase scheme

For further development, the model of Fig. 44 was associated with a thermodynamic scheme [58]. It includes four different phases:

- the amorphous melt
- mesomorphic layers (label 'm').

and, in order to account for the stabilization processes, two limiting forms of the crystallites, namely

- native crystals (label 'c<sub>n</sub>'),
- stabilized crystals (label 'c<sub>s</sub>').

The scheme, displayed in Fig. 46, delineates the stability ranges and transition lines for these phases. The variables in this phase diagram are the temperature and the crystal size, whereby the inverse crystal thickness serves as a size parameter. The thickness is given by the number  $n$  of structure units in a stem, i.e.  $n = d_c / \Delta z$ , with  $\Delta z$  denoting the stem length increment per structure unit. The transition lines are denoted  $T_{mcn}$ ,  $T_{acn}$ ,  $T_{mcs}$ ,  $T_{acs}$  and  $T_{amn}$ , all to be understood as functions of  $n^{-1}$ .

Of particular importance in the scheme are the 'crossing points'  $X_n$  and  $X_s$ . At  $X_n$  both mesomorphic layers and native crystalline layers have the same Gibbs free energy as the melt; at  $X_s$  the equality holds for the stabilized crystallites. The loci of points  $X_n$  and  $X_s$  control what happens during an isothermal crystallization followed by heating. There are two different scenarios, exemplified by the paths A and B in the figure; in experiments they are realized by crystallizations at low or high temperatures respectively. Path B: At the point of entry, labeled '1', chains are attached from the melt onto the lateral growth face of a mesomorphic layer with the minimum thickness. The layer spontaneously thickens until the transition line  $T_{mcn}$  is reached at point '2', where native crystals form immediately. The subsequent stabilization transforms them into a state of lower surface free energy. The consequence of the stabilization shows up during subsequent heating. Without stabilization, heating would immediately transform the native crystals back into the mesomorphic state, but after stabilization the situation has changed: since the crossing point is shifted to location  $X_s$ , the crystallites remain stable upon heating until the next transition line is reached. As shown by the scheme, this transition is now a direct melting without the interference of a mesomorphic phase. Pathway A: the beginning is the same—starting at point 1 with attachment of chain sequences onto a spontaneously thickening mesomorphic layer, then, on reaching  $T_{mcn}$ , the formation of native crystals, followed by stabilization. On heating, the stabilized crystals at first retain their structure. However, as shown in the scheme, at first the transition line  $T_{mcs}$  is reached, which relates to a transformation into the mesomorphic state instead of a crystal melting. The consequences that follow are obvious (3a–b): The same two steps are repeated again and again, first a transition into the mesomorphic phase and then a thickening until crystals form. The end of this

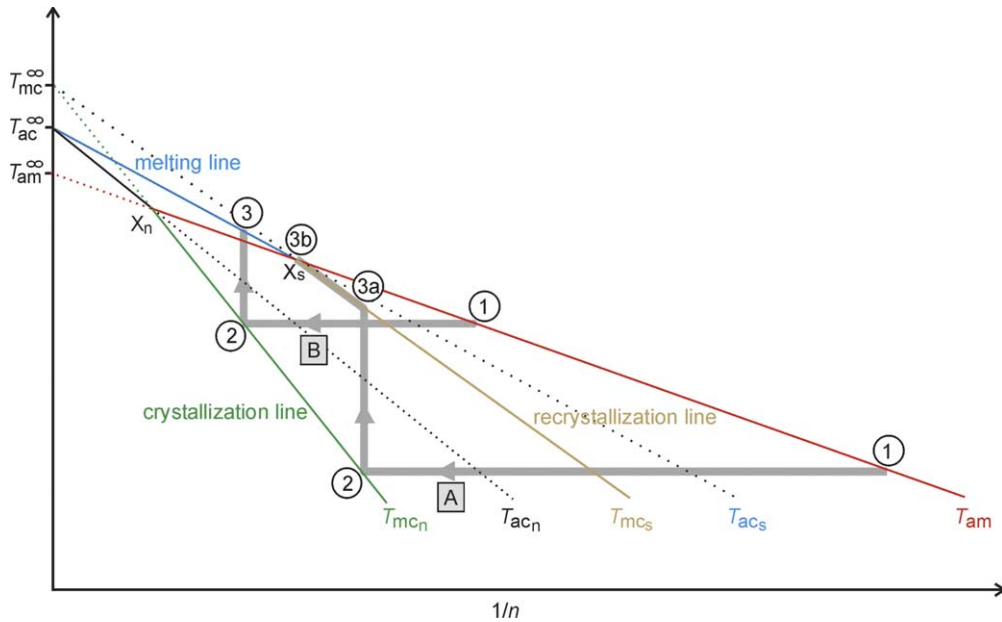


Fig. 46. Phase diagram,  $T$  versus.  $n^{-1}$ , for polymer layers in a melt ('a') dealing with three phases: mesomorphic 'm', native crystalline 'c<sub>n</sub>' and stabilized crystalline 'c<sub>s</sub>'. Two pathways for an isothermal crystallization followed by heating, A (low crystallization temperatures) and B (high crystallization temperatures). The experimental 'crystallization line' is identical with  $T_{mcn}$ , the 'melting line' is identical with  $T_{acs}$ , the 'recrystallization line' is to be identified with  $T_{mcs}$  [58].

multi-sequence process is reached at the crossing point  $X_s$  where the crystal melts.

Thermodynamics determines all the transition lines.  $T_{acs}$  relates to the equilibrium between stabilized crystals and the melt where

$$g_c + \frac{2\sigma_{acs}}{n} = g_a \quad (14)$$

$\sigma_{acs}$  denotes the surface free energy per crystal stem end for a stabilized layer in the melt. With

$$g_a - g_c \approx \frac{\Delta h_{ac}}{T_{ac}^{\infty}} (T_{ac}^{\infty} - T) \quad (15)$$

one obtains

$$T_{ac}^{\infty} - T \approx \frac{2\sigma_{acs}T_{ac}^{\infty}}{\Delta h_{ac}} \frac{1}{n} \quad (16)$$

In experiments, this line is called the 'melting line'. Proceeding in analogous manner one obtains for the 'crystallization line' the equation

$$T_{mc}^{\infty} - T \approx \frac{(2\sigma_{acn} - 2\sigma_{am})T_{mc}^{\infty}}{\Delta h_{mc}} \frac{1}{n} \quad (17)$$

and for the 'recrystallization line'

$$T_{mc}^{\infty} - T \approx \frac{(2\sigma_{acs} - 2\sigma_{am})T_{mc}^{\infty}}{\Delta h_{mc}} \frac{1}{n} \quad (18)$$

( $\sigma_{am}$  and  $\sigma_{acn}$  denote respective surface free energies). The transition between the melt and the mesomorphic state, described by the line  $T_{am}$ , occurs for

$$T_{am}^{\infty} - T \approx \frac{2\sigma_{am}T_{am}^{\infty}}{\Delta h_{am}} \frac{1}{n} \quad (19)$$

The line  $T_{am}(n^{-1})$  begins at  $T_{am}^{\infty}$  and then passes through the two crossing points  $X_n$  and  $X_s$ . A knowledge of two of these three points is required in order to fix the  $a \leftrightarrow m$  transition line.

### 9.3. Some applications

Figs. 32 and 34 demonstrate for sPP and PE with the related copolymers the independence of crystal thickness from co-unit content. Fig. 37 shows the effects of two different diluents for PEcO14, namely *n*-hexadecane and methylanthracene [23]. The results demonstrate that different diluents can act differently: dissolution of methylanthracene leaves the crystallization line unchanged, producing only a shift in the melting line, but dissolution of *n*-hexadecane results in shifts of both lines. The thermodynamic scheme provides understanding, and the two different situations are dealt with in Fig. 47 (from Ref. [58]). The effects depend on whether

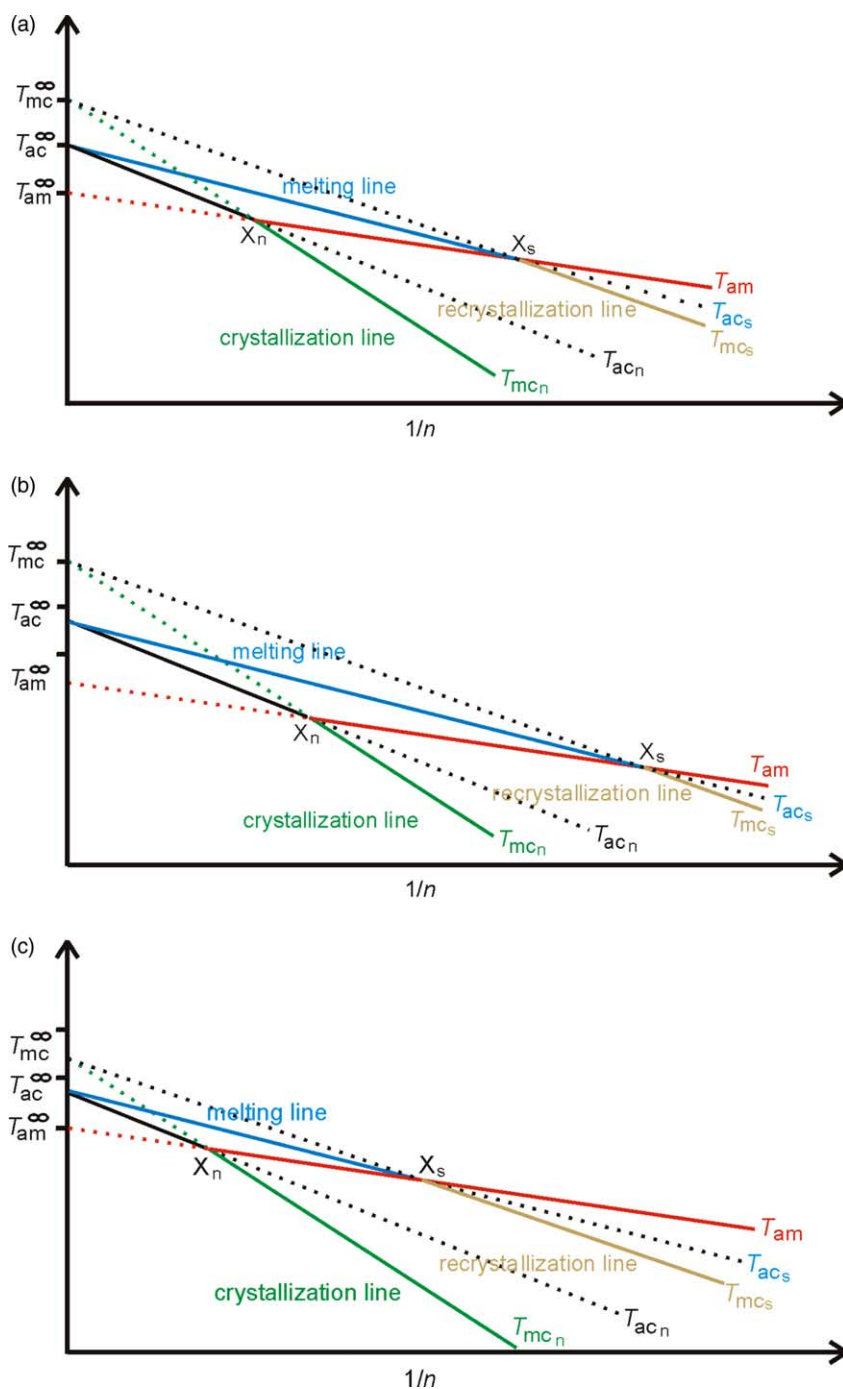


Fig. 47. Variations in the  $T/n^{-1}$  phase diagram due to co-units and diluents: (a) homopolymer crystallization; (b) effect of co-units or a diluent that remains in the melt (shifted melting line but invariant crystallization line); (c) effect of a diluent that enters the mesomorphic phase (shifts of both melting and crystallization lines) [58].

or not the diluent molecules or the co-units can enter the mesomorphic phase. If they are rejected, those transformation lines which include the melt, i.e.  $T_{acn}$ ,  $T_{acs}$  and  $T_{am}$ , are shifted to lower temperatures, but the line  $T_{mcn}$  remains unaffected. This is the situation sketched in part

b. The other situation is encountered if the diluent becomes incorporated into the mesomorphic phase and is only rejected subsequently when the crystals form. Under these conditions (part c) all transitions that include the crystalline state are shifted while

the transition between the melt and the mesomorphic phase,  $T_{am}$ , remains in place. Such a situation is obviously met if *n*-hexadecane is used as a diluent for PE, which leads to shifts of both the crystallization line  $T_{mcn}$  and the melting line  $T_{acs}$ .

The next examples concern the results of the SAXS and DSC studies on sPP and its copolymers reproduced in Figs. 31, 32 and 41 (from Ref. [58]). The SAXS data in Fig. 41 obtained for sPP-Mitsui are shown again in Fig. 48, but now with additional features referring to the scheme. The sample was cold crystallized from the melt at several temperatures between 100 and 120 °C. The thicknesses for the various crystallization processes are all located on the crystallization line. As mentioned previously, the changes in thickness with temperature observed during heating differ greatly. For the three highest temperatures, thicknesses remain constant up to the melting points. For the cold crystallized sample, changes set in immediately when heating is begun.  $d_c^{-1}$  approaches and then follows the recrystallization line, until melting occurs near or at the crossing point  $X_s$ . As is obvious, with crystallization at the three highest temperatures one enters pathway B of the scheme; for lower temperatures the structure changes during heating are those of pathway A. The temperature at the crossing point  $X_s$  appears also in the DSC scans on the right side in Fig. 41. After an extended range of continuous reorganization, which extends up to 110 °C, crystals melt at about 130 °C, in agreement with the location of  $X_s$  found in the SAXS experiments. The melting line has to pass through the measured melting points.

Fig. 49 collects SAXS data obtained for sPPcO20, already displayed in Figs. 31 and 32. The data fix the crystallization and melting lines well; and the line plotted through the three high temperature points—representing  $T_{acn}$ —determines  $X_n$ . An additional DSC scan on a cold-crystallized sample yielded the temperature coordinate of  $X_s$ , which turned out to be 80 °C. The now known locations of the two crossing points  $X_n$  and  $X_s$  allow us to draw the  $a \leftrightarrow m$  transition line. With this, the scheme is fully developed.

Having established the scheme for both samples, we derived all relevant thermodynamic data, as collected in Table 1. The heat of fusion  $\Delta h_{ac} = 7.7$  kJ/mol  $C_3H_6$  was taken from the literature. The heat of transition  $\Delta h_{am} = 5.8$  kJ/mol  $C_3H_6$  followed from a simple consideration based on Fig. 45. Thermodynamics relates the three transition temperatures  $T_{am}^\infty$ ,  $T_{ac}^\infty$ ,  $T_{mc}^\infty$  with the heats of transition  $\Delta h_{ac}$  and  $\Delta h_{am}$ . Since the slopes of  $\Delta g_{am}$  and  $\Delta g_{ac}$  are given by the entropy changes  $\Delta s_{am}$  and  $\Delta s_{ac}$ , respectively, one can write

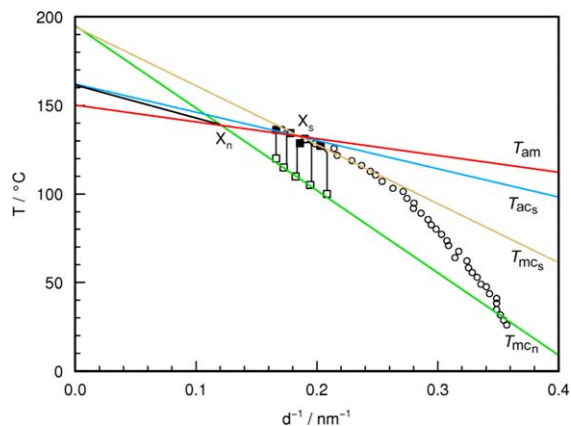


Fig. 48. sPP-Mitsui: SAXS data from Fig. 41 represented on the basis of the multiphase scheme. In addition to the crystallization line  $T_{mcn}$  and the melting line  $T_{acs}$ , the figure now includes the recrystallization line  $T_{mcs}$ , the  $a \leftrightarrow m$  transition line  $T_{am}$  and the crossing points  $X_n$  and  $X_s$  [58].

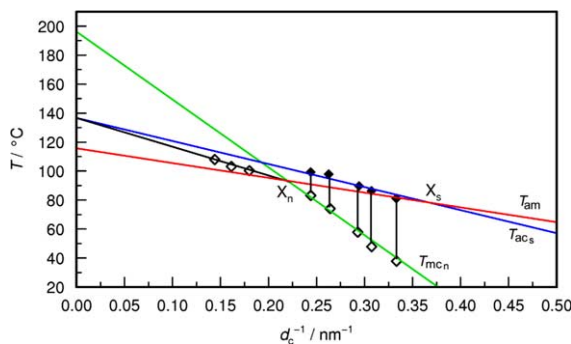


Fig. 49. SAXS data of sPPcO20 from Figs. 31 and 32: representation on the basis of the multiphase scheme, with crystallization line ( $T_{mcn}$ ), melting line ( $T_{acs}$ ), crossing points  $X_n$  and  $X_s$  and the  $a \leftrightarrow m$  transition line ( $T_{am}$ ) [58].

$$(T_{mc}^\infty - T_{ac}^\infty) \Delta s_{ac} = (T_{mc}^\infty - T_{am}^\infty) \Delta s_{am} \quad (20)$$

and, therefore, obtain

$$\frac{\Delta h_{am}}{\Delta h_{ac}} \approx \frac{\Delta s_{am}}{\Delta s_{ac}} = \frac{T_{mc}^\infty - T_{ac}^\infty}{T_{mc}^\infty - T_{am}^\infty} \quad (21)$$

The three surface free energies were derived from the slopes of the respective transition lines.

## 10. Metastable mesomorphic phases

As is evident, the consistency of the data representation in the framework of the proposed thermodynamic multiphase scheme corroborates its validity. It may be surprising that a mesomorphic phase with properties intermediate between the crystal and the melt should

Table 1  
*s*-Polypropylene and *s*-poly(propylene-*co*-octene): thermodynamic data following from the experiments

|            | $T_{mc}^{\infty}$<br>(°C) | $T_{ac}^{\infty}$<br>(°C) | $T_{am}^{\infty}$<br>(°C) | $T(X_n)$<br>(°C) | $T(X_s)$<br>(°C) | $\Delta h_{ac}$ (kJ/<br>mol C <sub>3</sub> H <sub>6</sub> ) | $\Delta h_{am}$ (kJ/<br>mol C <sub>3</sub> H <sub>6</sub> ) | $\sigma_{can}$ (kJ/mol) | $\sigma_{acs}$ (kJ/mol) | $\sigma_{am}$ (kJ/mol) |
|------------|---------------------------|---------------------------|---------------------------|------------------|------------------|---|---|-------------------------|-------------------------|------------------------|
| sPP-Mitsui | 195                       | 162                       | 150                       | 139              | 132              | 7.7   | 5.8   | 9.0                     | 7.5                     | 3.4                    |
| sP(PcO20)  | 195                       | 137                       | 113                       | 92               | 80               | 7.7   | 5.8   | 9.0                     | 7.5                     | 3.4                    |

exist for all polymer systems thus far investigated, but the experiments indicate it. For some systems the mesomorphic phase shows up directly, and we review here the relevant observations for polyethylene and *s*-polypropylene.

### 10.1. The hexagonal phase of polyethylene

For pressures above 3.2 kb, the mesomorphic, hexagonal phase appears in polyethylene as a stable phase, in addition to the orthorhombic-crystalline and the liquid phase. In this high pressure range, cooling from the melt leads at first into the stability range of the hexagonal phase before, on further cooling, the crystalline state is reached. If a sample is kept in the stability range of the hexagonal phase, thin layers spontaneously thicken to macroscopic sizes. When the transition into the crystalline phase is induced by cooling after a prolonged thickening period, one ends up with the nearly completely crystalline, banded ‘extended chain morphology’ of polyethylene. The extended chain morphology thus represents the signature of a passage through the mesomorphic phase. Fig. 50 shows this morphology; however, in this case, it was not obtained by the high pressure crystallization and cooling procedure. Tracz et al. [62] crystallized a film of high density polyethylene by cooling a melt in contact with a surface of freshly cleaved, oriented pyrolytic graphite. After detachment of the film from the substrate, the contact plane was scanned by AFM. The striations within the bands are uniformly oriented and indicate the common chain direction. This finding means that the interaction forces between PE and the graphite surface were strong enough to stabilize the mesomorphic phase within a surface layer so that the passage through this intermediate phase was much prolonged.

Fig. 51 presents some optical micrographs from recent work of Rastogi et al. [63] which also deals with the crystallization of PE under elevated pressures close to the triple point at 3.2 kb. The change in the appearance of the arrowed crystal indicates the transition from the hexagonal phase, which is first formed, to the orthorhombic crystalline phase. With the transition, the growth of the hexagonal entity is arrested.

The transition occurs statistically, whereby the mean residence time in the hexagonal phase decreases when the temperature is lowered. Furthermore, it is noted that the transformed crystals act as nucleation centers for many new crystals. Finally, there results a multicrystal cluster.

An intermediate phase between the crystalline state and the melt is also found in *n*-alkanes for chains with less than about 40 carbon atoms. The stability range as it shows up during heating or cooling is of the order of a few degrees. It is usually called a ‘rotator phase’, since chain reorientation about the long axis constitutes the main aspect of disorder. The rotator phase of *n*-alkanes is more crystal-like than liquid-like, differing from the hexagonal phase of PE, which is closer to the liquid. There also exist peculiar cases in which a mesomorphic phase is also found for polyethylene at normal pressures. This occurs when the chains are chemically modified by irradiation, or if a mechanical field is applied to ultrahigh molar mass polyethylene fibers, so that the shrinkage which usually accompanies the melting is at first suppressed [64]. From these findings, the question arises whether or not all these intermediate phases are related, in the sense that their character changes continuously from the rotator phase of the *n*-alkanes to the hexagonal phase of a polyethylene at high pressures and

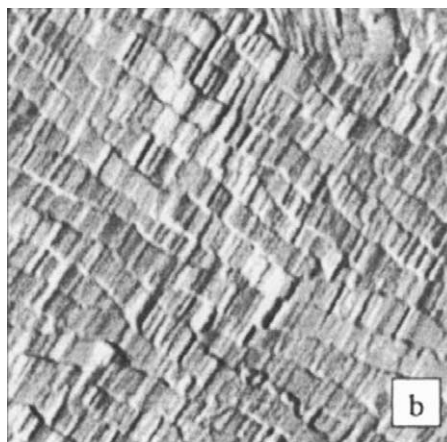


Fig. 50. LPE crystallized by cooling a melt in contact with a graphite surface (cooling rate, 10 K min<sup>-1</sup>): AFM tapping-mode phase image of the contact plane (1 μm scan). Reproduced with permission from Tracz et al. [62]. Copyright (2002) Wiley Periodicals Inc.

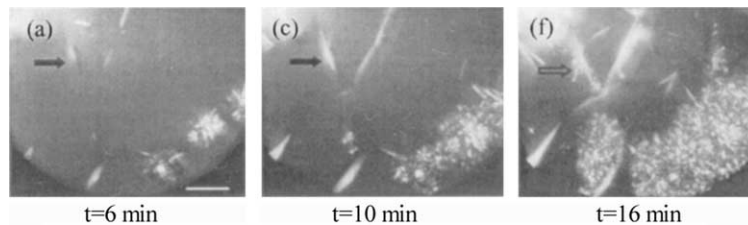


Fig. 51. LPE,  $M=32,000$ , isothermal crystallization under an applied pressure of 3.2 kbar observed with a polarizing microscope. Different stages of crystal development. Initiation and growth in the hexagonal phase and transition to the orthorhombic phase, which stops the growth. Transitions are indicated by a change in the appearance of the crystallites (arrowed crystal: transition between (c) and (f)). Reproduced with permission from Rastogi et al. [63].

temperatures. Ungar dealt with this question in a thorough analysis based, in particular, on vibrational spectroscopy. He arrived at the conclusion that there is only one mesomorphic phase [65]. There is a continuous change in the conformational statistics when going from short chain  $n$ -alkanes to longer chain  $n$ -alkanes, then to irradiated and fixed-length polyethylene and, finally, taking into account the associated high temperature, to the hexagonal high pressure phase of polyethylene. Fig. 52, taken from Ungar's work, depicts the results obtained for normal pressures. It shows the stability ranges of the mesomorphic phase of  $n$ -alkanes, irradiated polyethylene and a fixed-length ultrahigh molar mass polyethylene. The upper boundary always gives the transition line between the melt and the mesomorphic phase, and the lower boundary that between the mesomorphic phase and the crystalline state.

It is obvious that there is a smooth continuation from the  $n$ -alkanes to polyethylene. When the crystallization line and the melting line of PE are plotted on Ungar's phase diagram, noteworthy results become apparent [58]. The first interesting observation concerns the melting points. Comparing crystalline layers with the same thickness  $n$ , it is found that the  $n$ -alkanes melt at much lower temperatures than polyethylene (dotted line in Fig. 52). The reason follows from the analysis carried out by Flory and Vrij [66]. Polyethylene crystals with thickness  $n$  melt when

$$ng_c + 2\sigma_{ac} = ng_a \quad (22)$$

where  $\sigma_{ac}$  denotes the surface free energy per crystalline stem end. For  $n$ -alkanes the Gibbs free energy per molecule in the melt is further reduced by delocalization of the  $\text{CH}_3$  endgroups. This changes the equilibrium

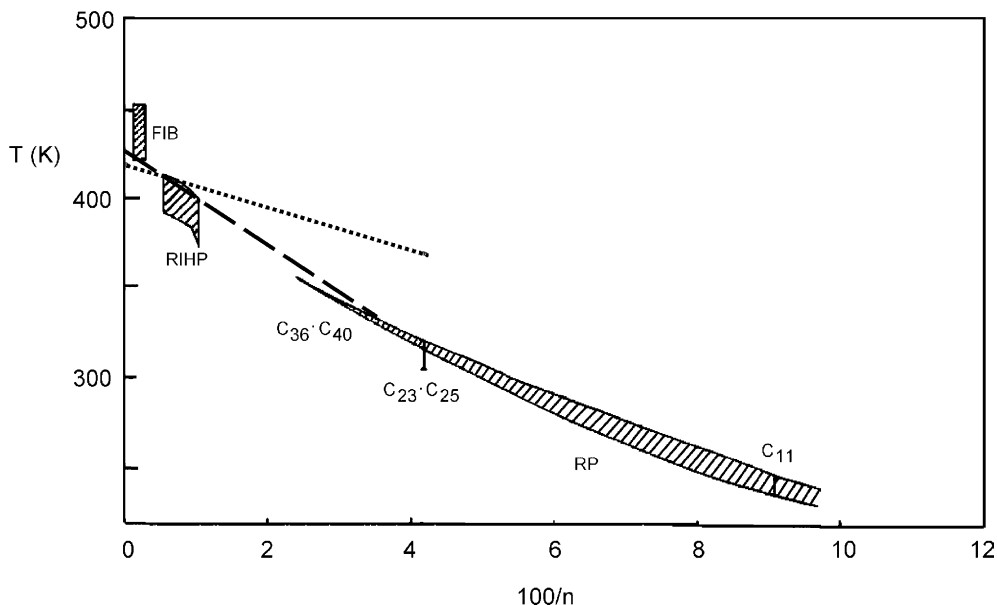


Fig. 52. Stability ranges of the mesomorphic phase, for various  $n$ -alkanes (rotator phase 'RP'), irradiated polyethylene (radiation-induced hexagonal phase 'RIHP'), and a fixed-length ultrahigh molar mass PE fiber ('FIB');  $n$  is the number of carbons in the molecule or crystal stem (from Ungar [65]). Crystallization line (broken) and melting line (dotted) of PE from Fig. 34.

condition at the melting point of *n*-alkanes to

$$ng_c + 2\sigma_{ac} = ng_a - RT \ln n. \quad (23)$$

Flory and Vrij derived from *n*-alkane melting point data a value of  $13 \text{ kJ mol}^{-1}$  for  $2\sigma_{ac}$ , which agrees with the value derived from the slope of the PE melting line ( $13.1 \text{ kJ mol}^{-1}$ ). The close approach of the hexagonal-melt to the orthorhombic–hexagonal transition in the *n*-alkane phase diagram is thus due to the translational entropy contribution alone. Since the latter is absent in the melting process of polyethylene, the stability range for mesomorphic polyethylene layers with thicknesses in the nanometer range—comparable to the *n*-alkanes—becomes much expanded. Hence, thin mesomorphic PE layers are indeed stable objects under normal pressure. The second noteworthy finding concerns the crystallization line. As can be seen, it nearly coincides at first with the mesomorphic–crystalline phase transition of the *n*-alkanes and then continues it. Since the endgroup location in the interfaces of the *n*-alkane crystal is retained in this transition, no translational entropy arises and there is no difference between polyethylene and *n*-alkane layers. The observed coincidence therefore leads to an important conclusion: namely, that the crystal thickness  $d_c$  is selected exactly by this transition.

Even if the mesomorphic phase is only metastable for some *n*-alkanes, it still contributes to their crystallization properties. Sirota et al. investigated the nucleation of various *n*-alkanes and Fig. 53 reproduces an interesting result [67]. WAXS patterns recorded for *n*-C<sub>16</sub>H<sub>34</sub> during the onset of crystallization clearly show that the system nucleates into the rotator-phase—which is here metastable—before it converts to the stable triclinic crystal modification. This is not a peculiarity of this compound. As it turns out, the undercooling associated with the homogeneous nucleation of *n*-alkanes is generally determined by the temperature of the phase transition from the melt into the rotator phase, rather than into the crystal phase. This route via an intermediate state is always much faster. Ostwald's rule of stages also applies here.

The experimental results in Fig. 54 suggest that this route for nucleation might be followed by polyethylene as well (from Sirota et al. [68]). The supercooling  $\Delta T$  measured at the onset of homogeneous nucleation varies smoothly between the *n*-alkanes and PE. To explain the increase of  $\Delta T$ , beginning with *n*-alkanes with a length of about 25 CH<sub>2</sub> groups and then increasing to 58 °C for PE, Sirota et al. invoked a continuous crossover from a crystal block to a fringed-micelle type of nucleus.

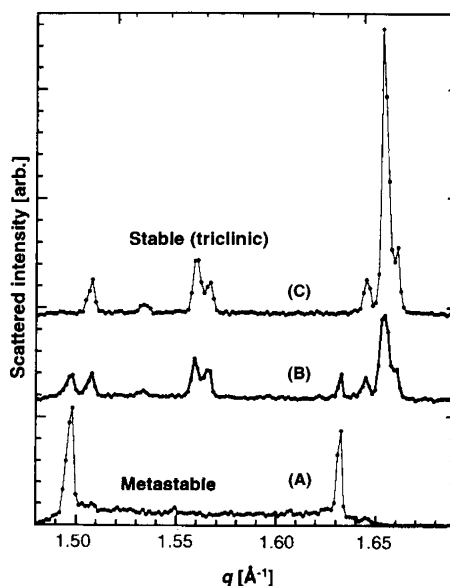


Fig. 53. *n*-C<sub>16</sub>H<sub>34</sub>, WAXS patterns obtained during crystallization on cooling: the metastable rotator phase (A) appears prior to the stable triclinic phase (C). Reproduced with permission from Sirota et al. [67]. Copyright (1999) American Association for the Advancement of Science.

### 10.2. The *trans* mesophase of *s*-polypropylene

When glassy amorphous sPP is transferred from temperatures below  $T_g$  ( $-5^\circ\text{C}$ ) to a temperature below  $20^\circ\text{C}$  and is stored there for sufficient time, a mesomorphic phase develops together with the crystalline phase. Upon heating, the former disappears. Since the thicknesses of the two phases are equal and vary on heating in identical manner, we speculated that this

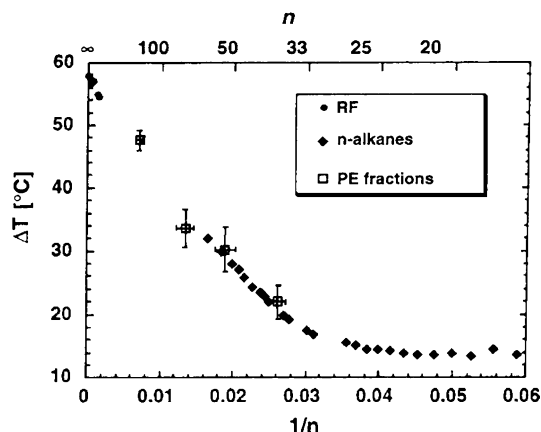


Fig. 54. *n*-Alkanes and PE crystallized by cooling the melt: temperatures of homogeneous nucleation, given by supercooling  $\Delta T$  below the respective equilibrium melting points. Reproduced with permission from Sirota et al. [68]. Copyright (2000) American Chemical Society.

mesomorphic phase could be identical with the intermediate phase which controls the crystallization of sPP [57].

The first reports about this phase came from Horii, Nakaoki et al. [69]. Both  $^{13}\text{C}$  NMR spectra and WAXS patterns recorded at  $0^\circ\text{C}$  indicated the development of a mesomorphic structure in which the chains are preferentially in the all-*trans* form. The development is very slow and requires some days. If it remains incomplete and the sample is brought to ambient temperatures earlier, crystalline layers form rapidly and then coexist with the mesomorphic layers. In a further study, Ohira et al. [70] found a conversion of the mesomorphic into the crystalline phase during heating and analyzed the change by WAXS and NMR. It sets in at  $20^\circ\text{C}$  and then extends up to  $100^\circ\text{C}$ , with the maximum conversion rate near the end.

Fig. 55, reproduced from a publication of Auriemma et al. [71], shows that mesomorphic and crystalline phases can also be easily distinguished in the IR spectrum. The bands assigned to the *trans* (T) and the helical (H) conformation are clearly separated. Using this differentiation, De Rosa et al. demonstrated that stereoregularity has a strong influence on the rate of formation of the mesomorphic phase [72]: the higher the syndiotacticity, the easier is its formation.

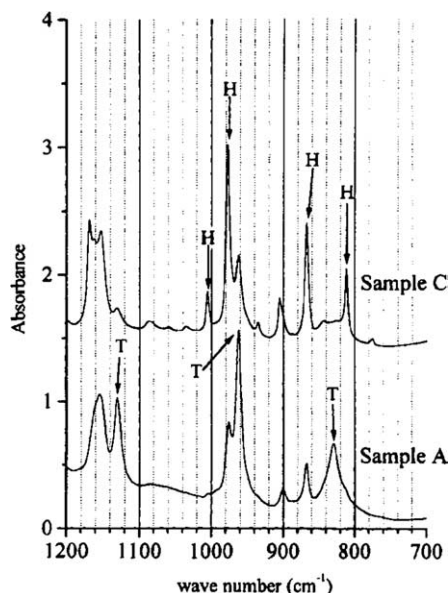


Fig. 55. sPP cold-crystallized for two months at  $0^\circ\text{C}$  (sample A) and subsequently annealed for 1 h at  $90^\circ\text{C}$  (sample C): IR spectra with bands characteristic of chains with helical (H) or *trans*-planar (T) conformation. Reproduced with permission from Auriemma et al. [71]. Copyright (2000) American Chemical Society.

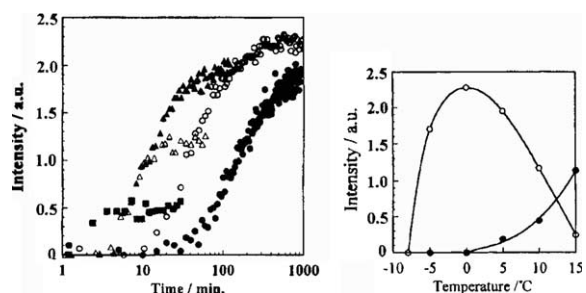


Fig. 56. sPP, cold-crystallization at five temperatures between  $-5$  and  $15^\circ\text{C}$ : (left) evolution of the *trans*-band at  $829\text{ cm}^{-1}$ . (right) Intensities of the *trans* band (open symbols) and of the helical band (filled symbols) in the final states. Reproduced with permission from Horii et al. [73]. Copyright (2000) American Chemical Society.

An evaluation of a time-dependent IR spectroscopic experiment led Nakaoki, Horii et al. [73] to the results shown in Fig. 56. The rate of formation of the mesomorphic phase increases with rising temperature while the fraction of chains finally incorporated in this phase has a maximum at  $0^\circ\text{C}$  and then steadily decreases. The final volume fraction of the crystalline phase increases with the crystallization temperature. Interestingly, as shown by De Rosa et al. in another IR spectroscopic study [74], the total fraction of the mesomorphic plus the crystalline phase remains constant at a value of 0.3. Fig. 57 reproduces this result.

Figs. 58 and 59 depict results from a time- and temperature-dependent SAXS investigation on a sample of sPP whose structure was formed at  $0$ ,  $8$  or  $25^\circ\text{C}$  (from Ref. [57]). Fig. 58 compares values of  $d_c$  at  $0^\circ\text{C}$ , where only the mesomorphic phase develops, with those at  $8^\circ\text{C}$ , where mainly crystallites form. The shape of the scattering curves are similar and indicate formation of

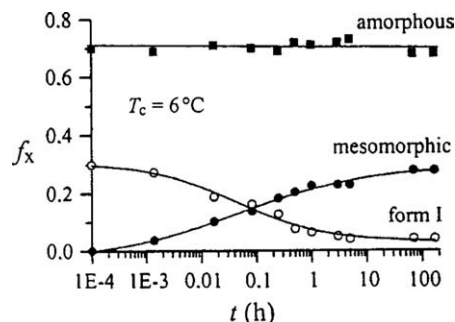


Fig. 57. sPP cold-crystallized at  $0^\circ\text{C}$  for various times  $t$  before a transfer to  $25^\circ\text{C}$ . Fractions  $f_x$  of the amorphous, *trans*-mesomorphic and helical (form I) phase as a function of time. Reproduced with permission from De Rosa et al. [74]. Copyright (2003) Elsevier Science Ltd.

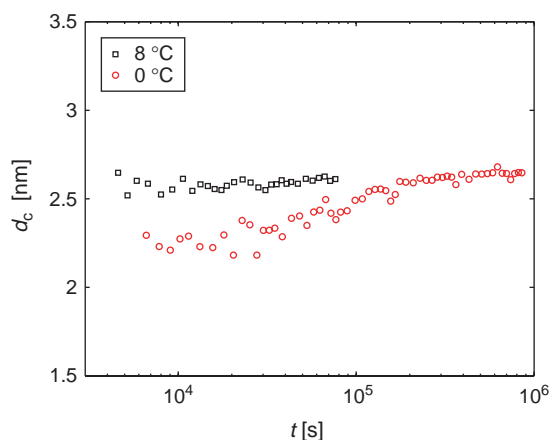


Fig. 58. sPP-Mitsui, crystallization at 0 °C (circles) and 8 °C (squares): time dependence of  $d_c$  derived from SAXS [57].

layers at both temperatures. The  $d_c$  data show thickening of the mesomorphic layers but a constant  $d_c$  for crystalline layers, and identical final values.

Fig. 59 depicts structural changes during heating for samples crystallized at 0 and 25 °C. There is complete

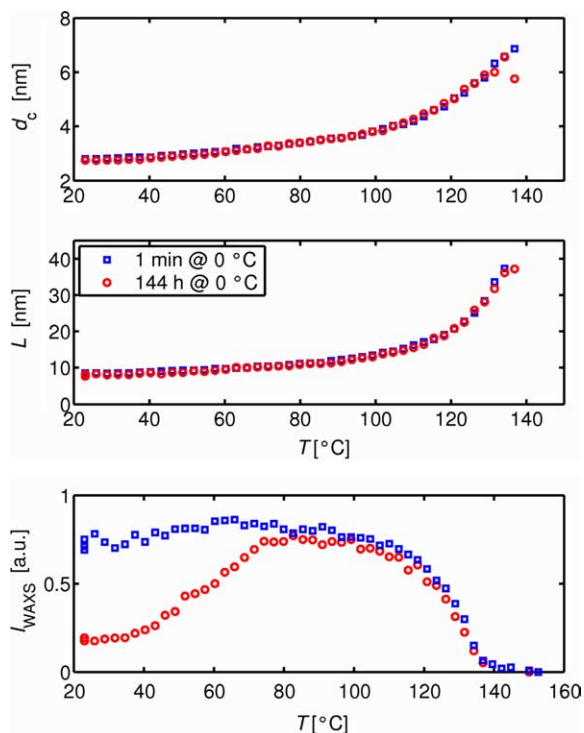


Fig. 59. sPP-Mitsui crystallized for several days at 0 °C (circles) and for one hour at 25 °C (squares). Changes of  $d_c$ , of the long spacing  $L$  and of the intensity of a Bragg reflection  $I_{WAXS}$  during heating from 25 °C to temperatures near the melting point [57].

agreement between the two samples for  $d_c(T)$  and the long spacing  $L(T)$ , i.e. the continuous reorganization took place in an identical manner. On the other hand, as shown by a Bragg reflection  $I_{WAXS}(T)$ , the mesomorphic phase was continuously converted into the crystalline phase.

## 11. Orientation by magnetic fields

The orienting effect of a magnetic field on a polymer melt is weak; even for strongly anisotropic macromolecules interaction forces are not strong enough to compete with the thermal energy of orientational segmental motions. Somewhat unexpectedly, under such circumstances, Kimura and co-workers could achieve high degrees of orientation for several polymers (poly(ethylene-naphthalate), PET, *i*-polystyrene) when they were crystallized in a strong magnetic field under appropriate conditions [75–77]. Speculating about the origin of this effect, the authors proposed that the alignment might take place during an induction period when an existing ordered mesophase could respond to a magnetic field, similarly to a liquid crystalline polymer.

An oriented texture of PET crystallites was achieved when a crystallized sample was heated to a temperature just above the melting point, then annealed for several minutes and cooled down by 20 °C to induce crystallization [77]. The crystallization was followed in real-time both with and without an applied magnetic field by measuring the intensity of light transmitted through crossed nicols. Fig. 60 shows the result. For the measurement in the magnetic field, an oscillation of the intensity  $I$  was observed. It indicates a continuous

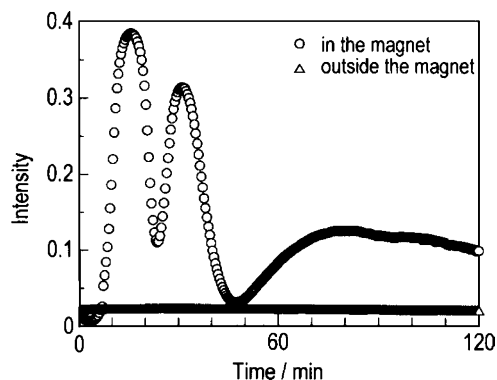


Fig. 60. PET crystallized in and without a magnetic field ( $B=6$  T) at 250 °C after melting at 270 °C: time dependence of the intensity of a light beam after passing through crossed nicols. Reproduced with permission from Kimura et al. [77]. Copyright (2000) Elsevier Science Ltd.

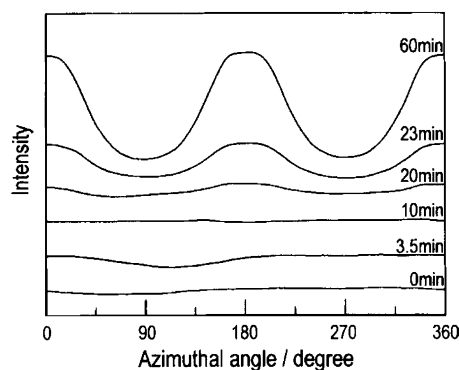


Fig. 61. Same sample as in Fig. 60. Azimuthal intensity distribution of the 100-reflection, measured after different crystallization times and quenching. Reproduced with permission from Kimura et al. [77]. Copyright (2000) Elsevier Science Ltd.

increase in the sample birefringence  $\Delta n$  which is related to the light intensity by

$$I \propto \sin^2(\pi t \Delta n / \lambda) \quad (24)$$

where  $t$  is the sample thickness and  $\lambda$  is the wavelength of light. The oriented crystal texture was further characterized by X-ray scattering experiments at room temperature for samples that had been quenched after different times of crystallization. Fig. 61 shows the development of the azimuthal intensity distribution of the 100-reflection. The normal vector of the 100-lattice planes becomes preferentially oriented perpendicular to the magnetic field. This implies the same orientation of the plane of the aromatic ring, for which the magnetic interaction energy is minimized.

Further insights into the condition leading to crystal orientation under the action of a magnetic field were obtained in the work of Ebert and Thurn-Albrecht on *i*-polystyrene (iPS) [78]. Fig. 62 reproduces optical micrographs of two spherulites which grew at 220 °C, one in a magnetic field, the other without it.

It can be seen that only the anisotropic hedritic core is oriented; the subsequent branching and splaying are not

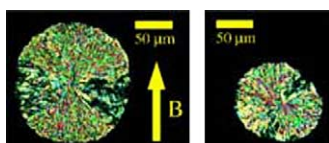


Fig. 62. iPS spherulites grown at 220 °C after cooling from the melt at 260 °C: optical micrographs (crossed polars) obtained after crystallization in (left) and without (right) the magnetic field  $B$ . Reproduced with permission from Ebert and Thurn-Albrecht [78]. Copyright (2003) American Chemical Society.

altered by the magnetic field. To obtain a macroscopically oriented crystal texture, the size of the spherulites has to be restricted so that the hedritic core represents the essential part of the spherulite. This requires a high nucleation density, which can be achieved by self-seeding, i.e. keeping the sample only shortly in the melt at a temperature just above the point of fusion. The authors estimated the time of rotation of a formed hedrite using the equation

$$\tau = \frac{6\eta\mu_0}{|\Delta\chi|B^2} \quad (25)$$

which is valid for a rigid sphere reorienting in a fluid matrix. Interestingly,  $\tau$  does not depend on the size of the rotating object, only on the anisotropy  $\Delta\chi$  of the magnetic susceptibility and the viscosity  $\eta$  of the fluid. The values of  $\tau$  thus determined are several orders of magnitude greater than the crystallization time. The authors therefore concluded that the alignment of the nucleus of the hedrite has to be assisted by a large internal mobility and an ability for inner rearrangements, as would be found in a transient non-crystalline phase.

## 12. Crystallinity

So far, our focus has been on lamellar crystallites, on the route followed in their formation, on their stability and melting. This, however, is only one part in the understanding of polymer crystallization. A further issue of first-rank importance asks about the crystallinity: how does it arise and what are the factors controlling it?

In a general view, the existence of a well-defined crystallinity and of orientational correlations between adjacent lamellae provides evidence that crystallites have interacted over mesoscopic distances during their evolution. Interaction forces control the distance between adjacent crystallites and thus determine the crystallinity, and they also establish the orientational correlations in the stacks. These forces have to be transmitted by the amorphous regions. Their topology, i.e. the chain entanglements, must play a decisive role. Under normal conditions, for ordinary molar masses and crystallization rates, the crystallization process does not resolve the entanglements. They are just moved into the amorphous regions and accumulate therein. As they cannot be resolved and, furthermore, opposing forces arise from their accumulation—the segmental mobility and therefore the entropy decrease—it is conceivable that the crystalline fraction cannot reach unity. However, these are just some rather obvious general ideas. As a matter of fact, a theory that can predict the

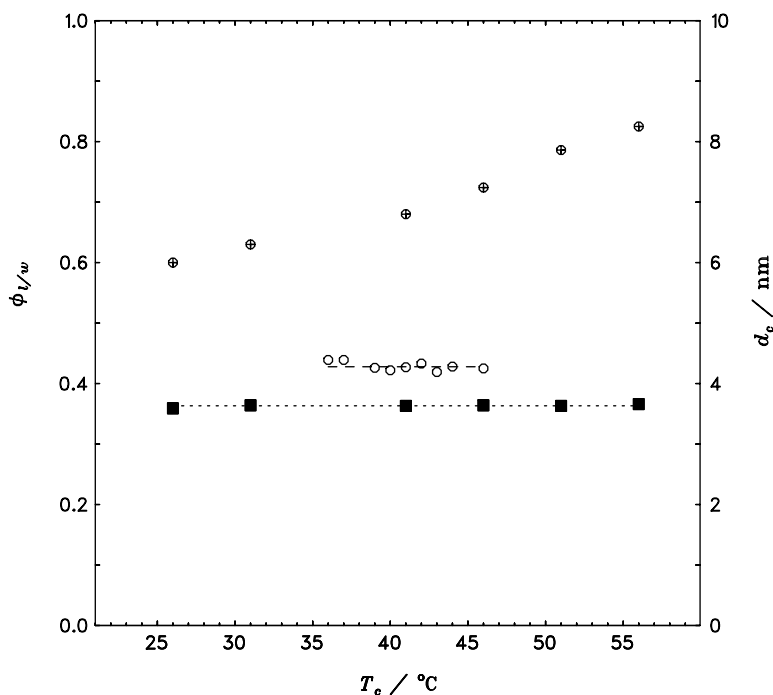


Fig. 63. Crystallinity of P $\epsilon$ CL after crystallization at different  $T_c$ s. Weight fraction crystallinity  $\phi_w$  derived from the DSC signal (open symbols) and linear crystallinity  $\phi_1$  determined by SAXS (filled symbols).  $T_c$  dependence of  $d_c$  (upper series with crossed symbols, referring to the right axis) [47].

crystallinity of a particular system, has not yet been developed.

SAXS, DSC and dilatometric investigations have revealed a simple rule: the crystallinity at the end of an isothermal crystallization process for a given polymer sample is invariant over a wide range of temperatures  $T_c$ . Figs. 63–65 reproduce results that were obtained for P $\epsilon$ CL, sPP, sPPcOx and PEcOx [47]. The crystallinity was always determined after the completion of a crystallization at the chosen  $T_c$ . It is evident that the final crystallinity is constant over a large  $T_c$  range. This is strictly true for the linear (SAXS) crystallinity  $\phi_1 = d_c/L$  and holds also for the DSC and dilatometric crystallinity for the majority of samples, as long as  $T_c$  is not too high. The observed decrease of the crystallinity of copolymerized samples at the highest  $T_c$ s is a necessity: the fraction of unperturbed chain sequences with the required length ( $\geq d_c$ ) finally drops below the constant value of the crystallinity found at lower temperatures. For comparison, the figures also include the  $T_c$  dependence of the crystal thickness; the length scales of the structures change quite remarkably.

The measurements confirmed that the crystallinity decreases when the co-unit content is increased, thereby indicated that this decrease is the result of an increase

in the interlamellar spacing only— $d_c$  remains unaffected. The same finding applies for the molar mass effect. The PEEK data, shown previously in Fig. 39, demonstrate that the thickness of the amorphous intercrystalline layer

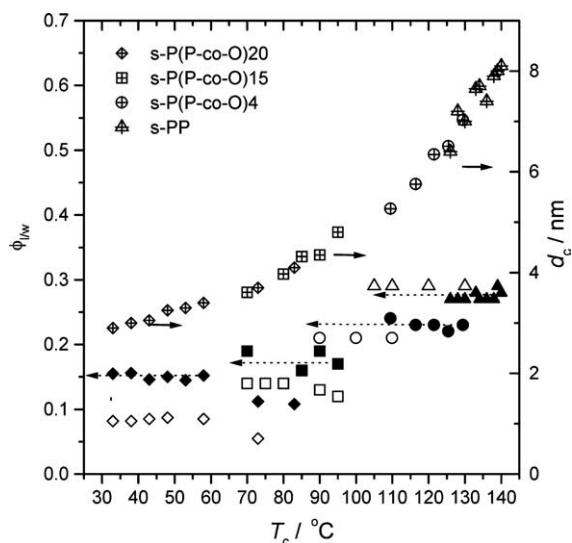


Fig. 64. Crystallinity of sPP and sPPcOx after crystallization at various  $T_c$ s: weight fraction crystallinity  $\phi_w$  derived from the DSC signal (open symbols) and linear crystallinity  $\phi_1$  determined by SAXS (filled symbols).  $T_c$  dependence of  $d_c$  (right axis) [47].

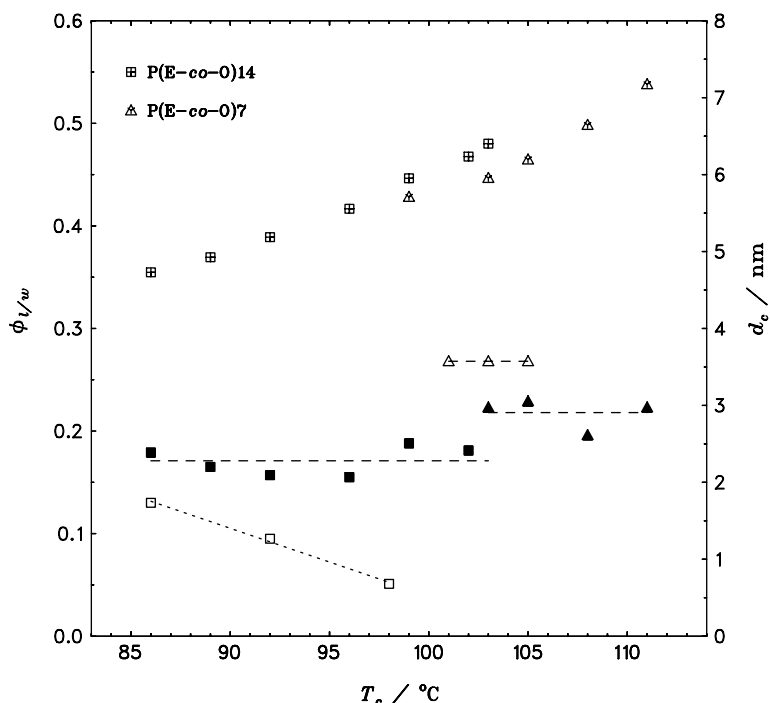


Fig. 65. Crystallinity of PEcOx after crystallization at different  $T_c$ s: weight fraction crystallinity  $\phi_w$  from dilatometry (open symbols) and linear crystallinity  $\phi_1$  from SAXS experiments (filled symbols).  $T_c$  dependence of  $d_c$  (right axis) [47].

varies while the crystal thickness is invariant. The data are in agreement with a suggestion by Rault [79] that the long spacing  $L$  might be proportional to the chain diameter  $R$  in the melt, i.e.

$$L \propto R \propto \sqrt{M}$$

The invariance of crystallinity for varying length scales of the structure implies that the amorphous regions always end up at the same entanglement density. Intuitively, this makes sense. The effects of co-units and molar mass show, however, that the entanglement density is only one of the controlling factors for the crystallinity. The molar mass dependence of  $L$  indicates that a chain that has already been included with one or more sequences in a crystallite will usually not be incorporated into another one—adjacent crystallites are thus kept apart at a distance on the order of the coil diameter.

Of course, the invariance of the crystallinity established at  $T_c$  does not imply a constant crystallinity after cooling to ambient temperature. On the contrary, crystallization always continues during cooling, and the increase resulting from this further crystallization is greater, the higher the  $T_c$  chosen.

### 13. Amorphous regions with reduced mobility

The presence of crystallites in semicrystalline polymers changes the properties of the amorphous regions. Only one part retains the mobility of the melt, for the other part—chain sequences near the surfaces of the crystallites—the mobility is reduced. Since the resulting density change is small, X-ray scattering experiments can still be evaluated by assuming a two-phase model, but experimental tools that probe differences in conformation or mobility can detect variations within the amorphous phase. Well established techniques for this purpose are NMR [80], Raman spectroscopy [81] and calorimetry [82]. Data evaluation requires here three components: in addition to the crystalline phase and the melt-like amorphous phase a third component, which is often called the ‘rigid amorphous fraction’. Since the mobility changes continuously between the crystal surface and the remaining melt-like regions, this third component does not represent a well-defined phase. The precise splitting of the amorphous region into two parts therefore depends on the experimental tool used. In the following, three selected recent experiments sensitive to mobility variations in the amorphous phase are discussed. They employ:

- temperature modulated calorimetry
- measurements of the solubility of a gas
- NMR in kinetical studies.

A reduction in mobility implies a decrease in entropy. As a consequence, forces arise which act on the crystals. Since these forces vary with temperature, equilibria at crystal surfaces can vary as well. For PE and PEO this results in a temperature-reversible surface crystallization and melting. A recent experiment, also presented in this section, was able to resolve the characteristic time for this process.

### 13.1. Characterization with mobility-sensitive techniques

Heat capacities measured for crystallized polymers by conventional DSC generally include, in addition to the basic phononic and rapid relaxation contributions, latent heats of crystallization and melting. A structural characterization requires only determination of the basic part. Schick et al. demonstrated that temperature modulated calorimetry (TMDSC), when carried out at an appropriate, not too low, frequency, provides this information and allows the rigid amorphous part in semicrystalline polymers to be determined [83]. For the latter it can be assumed that its basic heat capacity equals that of the glass. Fig. 66 reproduces results obtained for a sample of polycarbonate (PC). The figure on the left depicts the decay of the basic heat capacity  $|c_p^*|$ —determined by TMDSC—during isothermal crystallization at 457 K. The final value is much lower than expected for the given crystallinity

(here denoted  $X_{\text{CRF}}$ ): 22%, as derived from the heat of fusion. The difference is due to the presence of a rigid amorphous fraction, composed of 27% of the chains. This third component develops simultaneously with the crystallites.

How do the rigid amorphous parts react on heating? The answer is given by the data in Fig. 66 (right). Recrystallization begins 10 K above  $T_c$ , as indicated by the inset DSC curve at the bottom (right). The associated decrease in the crystallinity is small up to 490 K, however, the continuous reorganization is accompanied by a pronounced increase in the basic heat capacity  $|c_p^*|$ . At first, it rises to the value expected for a fully mobile amorphous phase (line d), and then it becomes even larger. It thus appears as if the mobility in the amorphous regions would increase until ‘rigid’ parts would no longer exist. Only if a very large residence time is chosen in the stepwise heating (10 h instead of 15 min), are the rigid parts in the amorphous phase preserved up to the main melting. Schick et al. described this increase in  $|c_p^*|$  as a ‘devitrification’ of the rigid amorphous phase.

Nazarenko et al. measured the oxygen solubility of PET for different degrees of crystallinity [84]. Some of their results are reproduced in Fig. 67. Since  $\text{O}_2$  does not enter the crystallites, a linear decrease of the solubility with the crystallinity  $S \propto (1 - \phi_c)$ , is expected. However, as shown by the curves in the left-hand plots, the actual decay is much smaller. The authors attributed this excess solubility to the presence of the rigid amorphous fraction. It is formed at the crystallization temperature  $T_c$  and obviously, on cooling to ambient temperature, maintains the higher free volume of the liquid at  $T_c$ . In this sense, there is a memory of  $T_c$ . Evaluation of

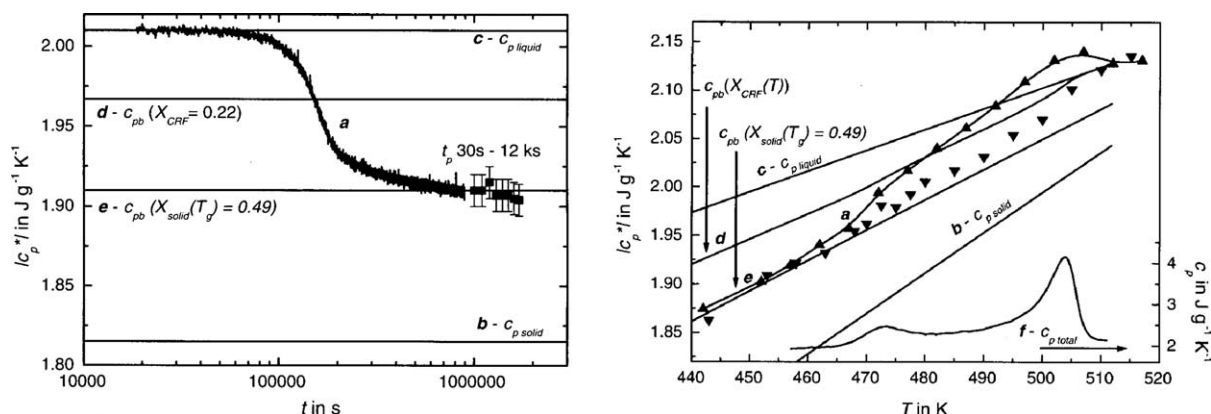


Fig. 66. PC, (left) crystallization at 457 K and (right) melting by stepwise heating with residence times of 15 min (▲) and 10 h (▼), studied by TMDSC (period  $\tau = 100$  s, amplitude  $\Delta T = 0.5$  K): (left) time and (right) temperature dependence of the modulus of the reversible heat capacity  $|c_p^*|$ . Horizontal lines (d) and (e):  $|c_p^*|$  as expected from the heat of fusion and the step at  $T_g$  respectively. Inset: DSC scan with a heating rate of 0.5 K min. Reproduced with permission from Schick et al. [83]. Copyright (2001) Springer-Verlag.

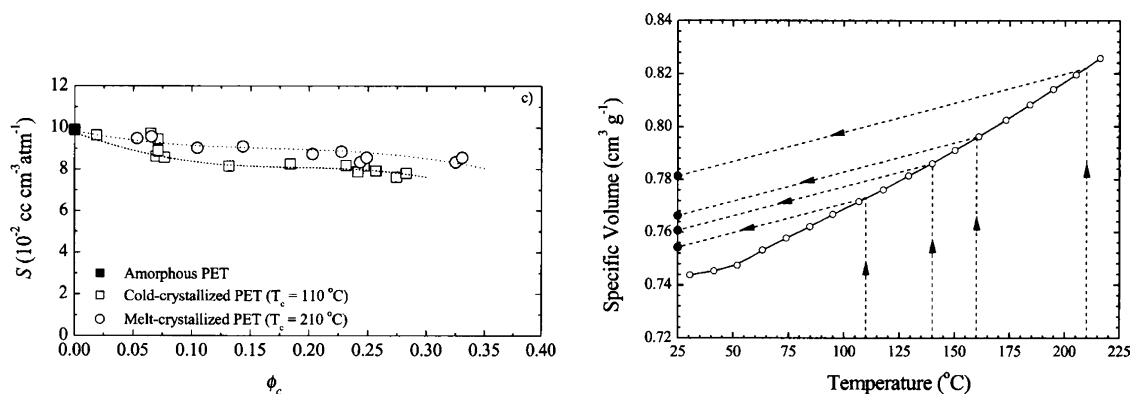


Fig. 67. PET with various crystallinities  $\phi_c$  prepared by cold crystallization at 110  $^\circ\text{C}$  and melt crystallization at 210  $^\circ\text{C}$  for various times: (left) variation of the solubility coefficient  $S$  for oxygen. (right) PET crystallized at four temperatures between 110 and 210  $^\circ\text{C}$ : specific volume of the rigid amorphous phase at 25  $^\circ\text{C}$  (filled circles). Reproduced with permission from Nazarenko et al. [84]. Copyright (2002) Elsevier Science Ltd.

solubility data for different  $T_c$  values and crystallinities enabled the specific volume of the rigid amorphous fraction at room temperature to be determined. The values that were found agree with those following from the construction in the plot on the right: i.e. the specific volumes can indeed be associated with glasses that vitrify at the chosen  $T_c$  values.

A particularly high sensitivity for detection of constraints on chain mobility in semicrystalline polymers is obtained in NMR experiments. Measurements of the free induction decay (FID) were used by Kristiansen et al. [85] and by us [86] to study the crystallization kinetics. Fig. 68 on the left reproduces one typical example: a set of FIDs  $A(\tau)$  recorded during the crystallization of P $\epsilon$ CL. The fast decay, which is already completed after  $2 \times 10^{-5}$  s, is assigned to the protons within the crystallites. The longest relaxation times are found for the protons in the remaining melt-like regions,

and these dominate the curve shape in the long-time asymptotic limit. The decay curves  $A_r(\tau)$  on the right were obtained after subtraction of the contributions of all protons with melt-like mobility and thus represent the temporal evolution of the signals attributed to all protons with reduced mobility. Splitting these empirically into contributions from the crystallites and the remaining part yielded for the time dependence of the three fractions the curves displayed in Fig. 69. Particularly interesting are the final values: the melt-like fraction drops to 10%, and is thus even smaller than the amorphous component with reduced mobility (35%).

### 13.2. Surface crystallization and melting in polyethylene

The surface crystallization and melting observed for PE and PEO—both are polymers where chains carry out sliding motions in the crystalline state—is a well

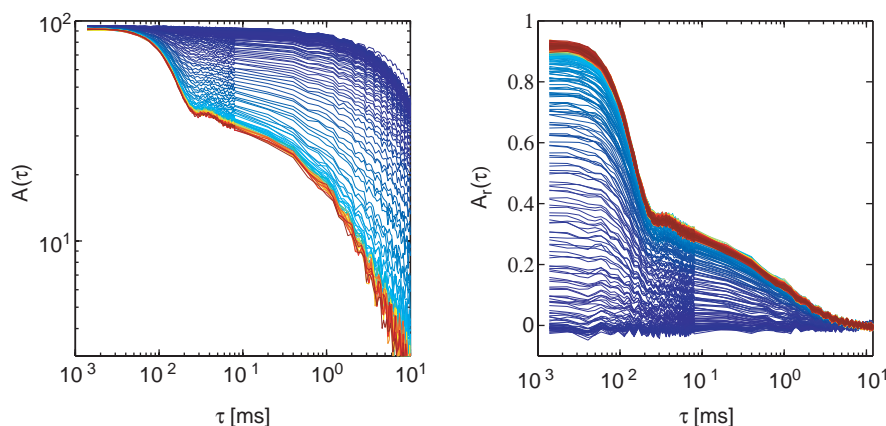


Fig. 68. P $\epsilon$ CL, crystallization at 51  $^\circ\text{C}$  studied by time-dependent  $^1\text{H}$  NMR. Measured FIDs  $A(\tau)$  (left) and the extracted component  $A_r(\tau)$  associated with protons with reduced mobility (right) [86].

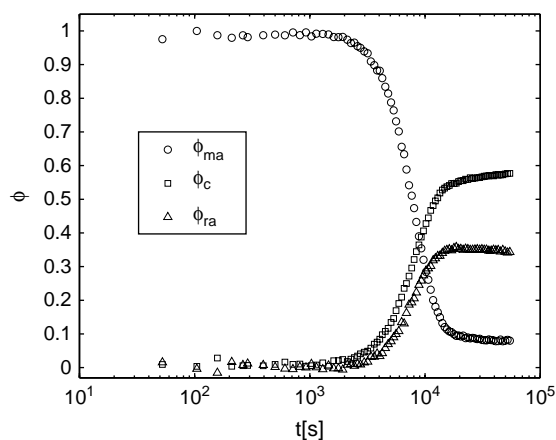


Fig. 69. P $\epsilon$ CL, crystallization at 51 °C, evaluation of the FIDs of Fig. 68: time dependence of the fractions associated with crystals ( $\phi_c$ ), amorphous regions with reduced mobility ( $\phi_{ra}$ ) and melt-like regions ( $\phi_{ma}$ ) [86].

understood phenomenon [22,87]. The sliding motion allows a shift of the crystalline–amorphous interface in response to a change in the interaction forces which act between the crystallites and the amorphous inter-crystalline regions. At each temperature, a new local equilibrium becomes established. After Hu et al. had demonstrated with TMDSC that this process is indeed fully reversible [88], temperature modulated calorimetry—complemented by heat wave spectroscopy (HWS)—was applied again to study the process dynamics [89]. Figs. 70 and 71 reproduce some major results, obtained for PE. Surface crystallization and melting shows up in the dynamic heat capacity  $c^*$  with a strong contribution that varies with the modulation frequency. Fig. 70 depicts this variation through the melting range. The frequency dependence of the signal

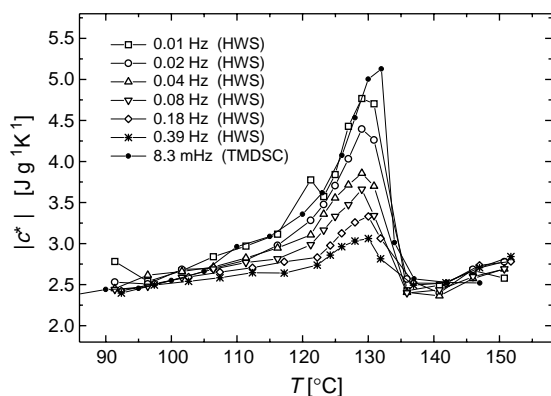


Fig. 70. PE studied by TMDSC and heat wave spectroscopy: temperature dependence of the modulus of the dynamic heat capacity measured for various frequencies [89].

amplitude indicates the relaxation time of the process. Here, it amounts to about 10 s—for a modulation period of 10 s the signal has dropped to half its initial value.

The first evidence of surface crystallization and melting came from SAXS measurements which showed a reversible change in the thickness of the amorphous layers [22,90]. The curves in Fig. 71 demonstrate perfect agreement between the previous SAXS results and the new TMDSC/HWS measurements.

Goderis et al., using a synchrotron radiation source, observed reversible changes in thickness of crystalline and amorphous layers in PE, which were caused by programmed temperature oscillations [33]. Fig. 72, taken from their work, depicts these thickness oscillations. The associated enthalpy fluctuations agreed with the amplitude of the excess part of the dynamic heat capacity determined by TMDSC. In principle, reversible crystallization and melting could also be initiated at the intralamellar grain boundaries [82], but this was not found and was excluded by the experiment.

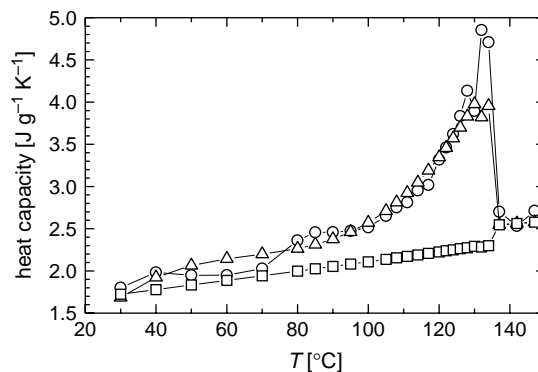
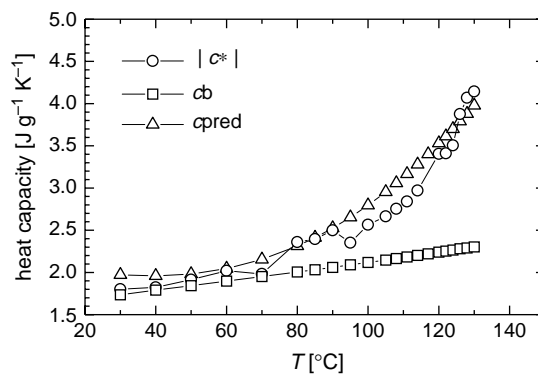


Fig. 71. PE, crystallized at 124 °C and annealed at 130 °C: dynamic heat capacity measured by TMDSC ( $t_p=240$  s) during cooling (top) and subsequent heating (bottom). The basic part  $c_b$  and total dynamic heat capacity  $c_{pred}$  predicted on the basis of the temperature variation of the crystallinity as determined by SAXS [89].

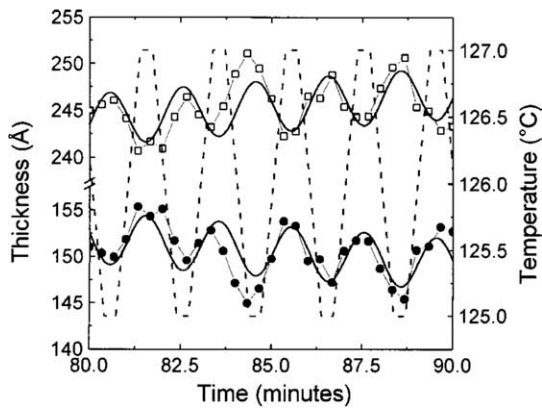


Fig. 72. PE, crystallized at 126 °C and then probed by temperature oscillations (period: 60 s, amplitude: 1 K): resulting variations of the crystal thickness (open squares) and the amorphous layer thickness (filled circles) as determined in a time dependence SAXS experiment. Reproduced with permission from Goderis et al. [33]. Copyright (2001) American Chemical Society.

#### 14. Growth rate

Temperature dependence measurements of growth rates were long considered as providing the primary information required for advancement of understanding of polymer crystallization. These were carried out using an optical microscope, and often also via measurements with other standard tools, assuming that the dominant factor is the strong exponential temperature dependence of the growth rate. Data interpretation was usually based on the Hoffman–Lauritzen theory, and the related parameters were derived.

As a matter of fact, the growth rate is not the well-defined, robust, simple property as it was treated by many. This was already indicated by Bassett's observations of a sequential buildup of spherulites, and is now the impression gained in AFM studies. A sequential buildup always begins with the fast growth of a few dominant lamellae and then continues with the much slower common growth of stacks of subsidiary lamellae. The drop in the growth velocity from the dominant to the subsidiary crystallites shows that growth rates are strongly affected by interactions between crystals. In this sense, growth rates represent in general a collective rather than an individual property.

AFM studies carried out by Hobbs et al. [91] and Chan, Li et al. [8] provided direct evidence for this effect. A constant growth rate was only found for advancing isolated lamellae: Fig. 73 depicts such an observation (from Ref. [8]). On the other hand,

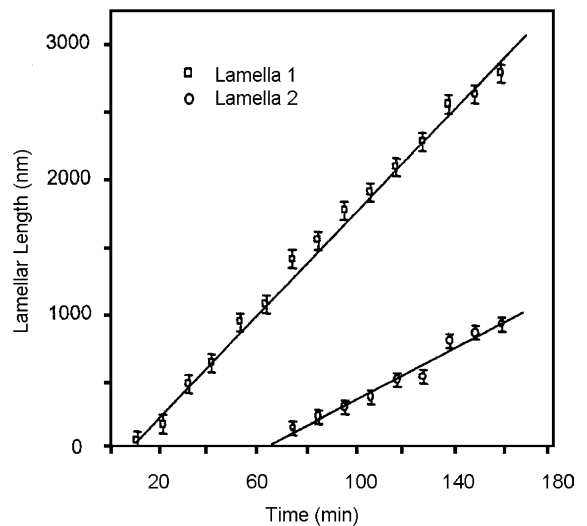


Fig. 73. BA-C8, crystallization at 22 °C observed by AFM: increase of the total lengths of the primary lamella grown out of the nucleus (1) and of a second lamella (2) which developed as a first branch. Reproduced with permission from Chan, Li et al. [8] Copyright (2003) Elsevier Science Ltd.

lamellae which grow together in a group always show strong variations in the growth rate, both temporal variations for one given lamella and fluctuations between different lamellae. Fig. 74 shows, as an example, observations by Hobbs et al. It is generally observed that the approach of one lamella to another slows the growth rate, even if they then grow in parallel. The growth rate as observed optically thus represents an average, but importantly, one that is affected by the proximity of the crystallites.

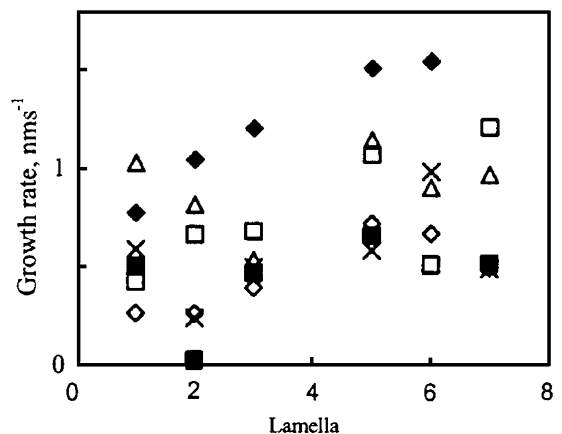


Fig. 74. PE, isothermal crystallization observed by AFM: growth rates measured for various lamellae (number 1–7) at various times. Evidence for fluctuations. Reproduced with permission from Hobbs et al. [91]. Copyright (2001) American Chemical Society.

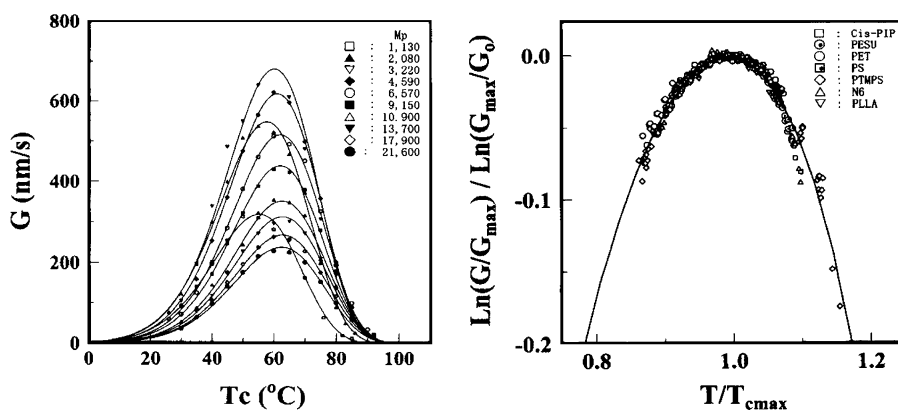


Fig. 75. (left) PESU fractions with various molar masses: temperature dependence of the spherulite growth rate. (right) Universal curve indicating a common temperature dependence of the growth rate for various polymers. Reproduced with permission from Okui et al. [92]. Copyright (2003) Springer-Verlag.

Interlamellar interactions can also be varied via the molar mass, whereby the lamellar thickness is kept constant (see the example Fig. 39). Fig. 75 shows growth rate measurements carried out by Okui et al. [92] for a set of fractions of poly(ethylene succinate) (PESU). For all but the two lowest molar masses (1130 and 2080 g mol<sup>-1</sup>) a clear trend shows up: The growth rate  $G$  drops in a systematic manner when the molar mass is increased. The authors describe the dependence by a power law,  $G(T_c) \propto M^{-\alpha} f(T_c)$ . The shape of the curve  $f(T_c)$ , is retained. The constancy of the shape reaches even further. The figure on the right compares  $G(T_c)$  curves measured for fractions in investigations of various polymer systems and demonstrates that  $f(T_c)$ , when plotted in reduced form, is virtually invariant.

### Acknowledgements

Support of our research in polymer crystallization and melting by the Deutsche Forschungsgemeinschaft is gratefully acknowledged. Invaluable contributions have been made by many of my former and present students and postdoctoral associates: Mahmud Al-Hussein, Simon Armbruster, Tai-Yon Cho, Jens Fritsch, Qiang Fu, Michael Grasruck, Andreas Häfele, Georg Hauser, Christoph Hertlein, Thomas Hippler, Wenbing Hu, Torsten Hugel, Masanori Iijima, Takahiko Kawai, Simon Keller, Peter Kohn, Eduard Sadiku, Jürgen Schmidtke, Werner Stille, Thomas Thurn-Albrecht. I would like to express here my appreciation for their work. The success of this research has surely been made possible by their unstinting commitment. Particular thanks are due to the technicians in our group, Barbara

Heck and Sylvia Siegenführ, and to my secretary Christina Skorek. Their ever reliable support—enthusiastically provided, with unfailingly high competence—has been an essential resource.

### References

- [1] Organization of macromolecules in the condensed phase. Faraday Discuss Chem Soc 1979:68.
- [2] Hoffman J, Davis G, Lauritzen J. The rate of crystallization of linear polymers with chain folding. In: Hannay NB, editor. Treatise on solid state chemistry, vol. 3. New York: Plenum Press; 1976. p. 497–614.
- [3] Keller A, Hikosaka M, Rastogi S, Toda A, Barham P, Goldbeck-Wood G. An approach to the formation and growth of new phases with application to polymer crystallization: effect of finite size, metastability, and Ostwald's rule of stages. J Mater Sci 1994;29: 2579–604.
- [4] Imai M, Kaji K, Kanaya T, Sakai Y. Ordering process in the induction period of crystallization of poly(ethylene terephthalate). Phys Rev B 1995;52:12696–704.
- [5] Olmsted P, Poon W, McLeish T, Terrill T, Ryan A. Spinodal assisted crystallization in polymer melts. Phys Rev Lett 1998;81: 373–6.
- [6] Hauser G, Schmidtke J, Strobl G. The role of co-units in polymer crystallization and melting: New insights from studies on syndiotactic poly(propene-co-octene). Macromolecules 1998;31: 6250–8.
- [7] Lei Y, Chan C, Li J, Ng K, Wang Y, Jiang Y, et al. The birth of an embryo and development of the founding lamella of spherulites as observed by atomic force microscopy. Macromolecules 2002;35: 6751–3.
- [8] Lei Y, Chan C, Wang Y, Ng K, Jiang Y, Li L. Growth process of homogeneously and heterogeneously nucleated spherulites as observed by atomic force microscopy. Polymer 2003;44:4673–9.
- [9] Vaughan AS, Bassett DC. Crystallization and morphology. In: Booth C, Price C, editors. Comprehensive polymer science, vol. 2. Oxford: Pergamon Press; 1989. p. 415–58.
- [10] Hobbs J. In-situ AFM of polymer crystallization. Chin J Polym Sci 2003;21:135–40.

- [11] Hobbs J. Following processes in synthetic polymers with scanning probe microscopy. In: Bateas JD, editor. Applications of scanned probe microscopy to polymers. Oxford: Oxford University Press; 2005. p. 194–206.
- [12] Kolb R, Wutz C, Stribeck N, von Krosigk G, Riekel C. Investigation of secondary crystallization of polymers by means of microbeam X-ray scattering. *Polymer* 2001;42:5257–66.
- [13] Kohn P. Die Entstehung von Lamellen in Polymeren während der Kristallisation. Freiburg, Institut für Physik, Universität Freiburg, Diplomarbeit; 2004.
- [14] Häfele A, Heck B, Kawai T, Kohn P, Strobl G. Crystallization of a poly(ethylene-co-octene): a precursor structure and two competing mechanisms. *Eur Phys J E* 2005;16:207–16.
- [15] Heck B, Kawai T, Strobl G. Time dependent light attenuation measurements used in studies of the kinetics of polymer crystallization. *Polymer*; in press.
- [16] Fritsch J, Stille W, Strobl G. Investigation of polymer crystallization kinetics with time-dependent light attenuation measurements. *Colloid Polym Sci*; in press.
- [17] Alfonso G, Ziabicki A. Memory effects in isothermal crystallization 2. Isotactic polypropylene. *Colloid Polym Sci* 1995;273: 317–23.
- [18] Heck B, Strobl G. Crystallization of *s*-polypropylene: a qualitative change in the kinetics induced by the temperature of the melt. *Colloid Polym Sci* 2004;282:511–3.
- [19] Häfele A, Heck B, Hippler T, Kawai T, Kohn P, Strobl G. Crystallization of poly(ethylene-co-octene): melt memory effects on first order kinetics. *Eur Phys J E* 2005;16:217–24.
- [20] Flory P. Theory of crystallization of polymers. *Trans Faraday Soc* 1955;51:848–70.
- [21] Ruland W. Evaluation of small angle X-ray scattering by means of interface distribution functions. *Colloid Polym Sci* 1977;255: 417–27.
- [22] Albrecht T, Strobl G. Temperature dependent crystalline—amorphous structures in linear polyethylene: surface melting and the thickness of the amorphous layers. *Macromolecules* 1995; 28:5827–33.
- [23] Heck B, Strobl G, Grasruck M. Characteristic variations in the effect of diluents on polymer crystallization and melting observed for a sample of poly(ethylene-co-octene). *Eur Phys J E* 2003;11: 117–30.
- [24] Patel D, Bassett DC. On spherulitic crystallization and the morphology of melt-crystallized poly(4-methylpentene-1). *Proc R Soc Lond A* 1994;445:577–95.
- [25] Ivanov D, Amalou Z, Magonov S. Real-time evolution of the lamellar organization of poly(ethylene terephthalate) during crystallization from the melt: high-temperature atomic force microscopy study. *Macromolecules* 2001;34:8944–52.
- [26] Cho T, Heck B, Strobl G. Equations describing lamellar structure parameters and melting points of polyethylene-co(butene/octene)s. *Colloid Polym Sci* 2004;282:825–32.
- [27] Hu W, Schmidt-Rohr K. Polymer ultradrawability: the crucial role of  $\alpha$ -relaxation chain mobility in the crystallites. *Acta Polym* 1999;50:271–85.
- [28] Hugel T, Strobl G, Thomann R. Building lamellae from blocks: the pathway followed in the formation of crystallites of syndiotactic polypropylene. *Acta Polym* 1999;50:214–7.
- [29] Hugel T. Lamellenbildung in teilkristallinen Polymeren. Freiburg Institut für Physik Universität Freiburg, Diplomarbeit; 1999.
- [30] Magonov S, Godovsky Y. Atomic force microscopy part 8: visualization of granular nanostructure in crystalline polymers. *Am Lab* 1999;31:52–8.
- [31] Ivanov D, Magonov S. Atomic force microscopy studies of semicrystalline polymers at variable temperature. In: Reiter G, Sommer JU, editors. Polymer crystallization, Lecture notes in physics. Berlin: Springer; 2003. p. 98–129.
- [32] Loos J, Thüne PC, Lemstra PJ, Niemantsverdriet WJ. Polymerization and crystallization of polyethylene on a flat model catalyst. *Macromolecules* 1999;32:8910–3.
- [33] Goderis B, Reynaers H, Scharrenberg R, Mathot V, Koch M. Temperature reversible transitions in linear polyethylene studied by TMDSC and time-resolved, temperature-modulated WAXD/SAXS. *Macromolecules* 2001;34:1779–87.
- [34] Yang Y, Geil P. Deformation mechanisms of isotactic poly(1-butene). *Makromol Chem* 1985;186:1961–78.
- [35] Hiss R, Hobeika S, Lynn C, Strobl G. Network stretching slip processes and fragmentation of crystallites during uniaxial drawing of polyethylene and related copolymers. A comparative study. *Macromolecules* 1999;32:4390–403.
- [36] Bassett DC, Patel D. Isothermal lamellar thickening and the distribution of thermal stability in spherulitic isotactic poly(4-methylpentene-1). *Polymer* 1994;35:1855–62.
- [37] Ivanov DA, Hocquet S, Dosière M, Koch M. Exploring the melting of a semirigid-chain polymer with temperature-resolved small angle X-ray scattering. *Eur Phys J E* 2004;13:363–78.
- [38] Liu T, Petermann J, He C, Liu Z, Chung T. Transmission electron microscopy observations on lamellar melting of cold-crystallized isotactic polystyrene. *Macromolecules* 2001;34:4305–7.
- [39] Jiang Y, Jin X, Han C, Li L, Wang Y, Chan C. Melting behaviors of lamellar crystals of poly(bisphenol A-co-decane ether) studied by in-situ atomic force microscopy. *Langmuir* 2003;19:8010–8.
- [40] Wurm A, Schick C. Development of thermal stability of polymer crystals during isothermal crystallization. *e-Polymers* 2002;024.
- [41] Jiang Y, Gu Q, Li L, Shen D, Jin X, Chan C. Conformational changes in the induction period of crystallization as measured by FT-IR. *Polymer* 2003;44:3509–13.
- [42] Noda I. Generalized 2-dimensional correlation method applicable to infrared, Raman, and other types of spectroscopy. *Appl Spectrosc* 1993;47:1329–36.
- [43] Noda I, Dowrey A, Marcott C, Story G, Ozaki Y. Generalized two-dimensional correlation spectroscopy. *Appl Spectrosc* 2000; 54:236A–248.
- [44] Padermshoke A, Sato H, Katsumoto Y, Ekgasit S, Noda I, Ozaki Y. Crystallization behavior of poly(3-hydroxybutyrate-co-3-hydroxyhexanoate) studied by 2D IR correlation spectroscopy. *Polymer* 2004;45:7159–65.
- [45] Zhang J, Duan Y, Shen D, Yan S, Noda I, Ozaki Y. Structure changes during the induction period of cold crystallization of isotactic polystyrene investigated by infrared and two-dimensional infrared correlation spectroscopy. *Macromolecules* 2004; 37:3292–8.
- [46] Kohn P, Strobl G. Continuous changes in the inner order of the crystalline lamellae during isothermal crystallization of poly( $\epsilon$ -caprolactone). *Macromolecules* 2004;37:6823–6.
- [47] Heck B, Hugel T, Iijima M, Sadiku E, Strobl G. Steps in the transition of an entangled polymer melt to the partially crystalline state. *New J Phys* 1999;1:17.1–17.29.
- [48] Iijima M, Strobl G. Isothermal crystallization and melting of isotactic polypropylene analyzed by time- and temperature dependent small angle X-ray scattering experiments. *Macromolecules* 2000;33:5204–24.
- [49] Al-Hussein M, Strobl G. Strain-controlled tensile deformation behaviour of isotactic poly(1-butene) and its ethylene copolymers. *Macromolecules* 2002;35:8515–20.

- [50] Fu Q, Heck B, Strobl G, Thomann Y. A temperature- and molar mass-dependent change in the crystallization mechanism of poly(1-butene): transition from chain-folded to chain-extended crystallization. *Macromolecules* 2001;34:2502–11.
- [51] Strobl G. From the melt via mesomorphic and granular crystalline layers to lamellar crystallites: a major route followed in polymer crystallization? *Eur Phys J E* 2000;3:165–83.
- [52] Hippler T, Jiang S, Strobl G. Block formation during polymer crystallization. *Macromolecules* 2005;38:9396–7.
- [53] Lee B, Shin T, Lee S, Yoon J, Kim J, Youn H, et al. Time-resolved X-ray scattering and calorimetric studies on the crystallization behaviors of poly(ethylene terephthalate) (PET) and its copolymers containing isophthalate units. *Polymer* 2003;44:2509–18.
- [54] Dreezen G, Koch M, Reynaers H, Groeninckx G. Miscible binary blends of poly(ethylene oxide) and an amorphous aromatic polyamide (Aramid 34I): crystallization, melting behavior and semicrystalline morphology. *Polymer* 1999;40:6451–63.
- [55] Fougnyes C, Dosi re M, Koch MHJ, Roovers J. Morphological study and melting behavior of narrow molecular weight fractions of poly(acryl ether ether ketone) annealed from the glassy state. *Macromolecules* 1998;18:6266–74.
- [56] Al-Hussein M, Strobl G. The mechanisms of recrystallization after melting in syndiotactic polypropylene and isotactic polystyrene. *Eur Phys J E* 2001;6:305–14.
- [57] Grasruck M, Strobl G. Crystallization of s-polypropylene from the glassy state: indications for a multistage process. *Macromolecules* 2003;36:86–91.
- [58] Strobl G. A thermodynamic multiphase scheme treating polymer crystallization and melting. *Eur Phys J E* 2005;18:295–309.
- [59] Al-Hussein M, Strobl G. The melting line the crystallization line and the equilibrium melting temperature of isotactic polystyrene. *Macromolecules* 2002;35:1672–6.
- [60] Minakov A, Mordvintsev D, Schick C. Melting and reorganization of poly(ethylene terephthalate) on fast heating (1000 K/s). *Polymer* 2004;45:3755–63.
- [61] Rastogi S, Hikosaka M, Kawabata H, Keller A. Role of mobile phases in the crystallization of polyethylene 1. Metastability and lateral growth. *Macromolecules* 1991;24:6384–91.
- [62] Tracz A, Jeszka J, Kucinska I, Chapel J, Boiteux G, Kryszewski M. Influence of the crystallization conditions on the morphology of the contact layer of polyethylene crystallized on graphite: atomic force microscopy studies. *J Appl Polym Sci* 2002;86:1329–36.
- [63] Rastogi S, Kurelec L. Polymorphism in polymers; its implications for polymer crystallization. *J Mater Sci* 2000;35:5121–38.
- [64] Tsubakihara S, Nakamura A, Yasuniwa M. Melting and crystallization of ultra-high molecular weight polyethylene with appearance of hexagonal phase i. Melting processes of fibers under constrained state. *Polym J* 1996;28:489–95.
- [65] Ungar G. From plastic-crystal paraffins to liquid-crystal polyethylene: continuity of the mesophase in hydrocarbons. *Macromolecules* 1986;19:1317–24.
- [66] Flory P, Vrij A. Melting points of linear-chain homologs. The normal paraffin hydrocarbons. *J Am Chem Soc* 1963;85:3548–53.
- [67] Sirota E, Herhold A. Transient phase-induced nucleation. *Science* 1999;283:529–32.
- [68] Kraack H, Deutsch M, Sirota E. n-Alkane homogeneous nucleation: crossover to polymer behavior. *Macromolecules* 2000;33:6174–84.
- [69] Nakaoki T, Ohira Y, Hayashi H, Horii F. Spontaneous crystallization of the planar zigzag form of syndiotactic polypropylene at 0 °C. *Macromolecules* 1998;31:2705–6.
- [70] Ohira Y, Horii F, Nakaoki T. Crystal transformation behavior and structural changes of the planar zigzag form for syndiotactic polypropylene. *Macromolecules* 2000;33:5566–73.
- [71] Vittoria V, Guadagno L, Comotti A, Simonutti R, Auriemma F, De Rosa C. Mesomorphic form of syndiotactic polypropylene. *Macromolecules* 2000;33:6200–4.
- [72] De Rosa C, Auriemma F, Ballester O. Influence of the stereoregularity on the crystallization of the *trans* planar mesomorphic form of syndiotactic polypropylene. *Polymer* 2001;42:9729–34.
- [73] Nakaoki T, Yamanaka T, Ohira Y, Horii F. Dynamic FT-IR analysis of the crystallization to the planar zigzag form for syndiotactic polypropylene. *Macromolecules* 2000;33:2718–21.
- [74] De Rosa C, Ruiz de Ballesteros O, Santoro M, Auriemma F. Influence of the quenching temperature on the crystallization of the *trans* planar mesomorphic form of syndiotactic polypropylene. *Polymer* 2003;44:6267–72.
- [75] Sata H, Kimura T, Ogawa S, Yamato M, Ito E. Magnetic orientation of poly(ethylene-2,6-naphthalate). *Polymer* 1996;37:1879–82.
- [76] Sata H, Kimura T, Ogawa S, Yamato M, Ito E. Magnetic orientation of poly(ethylene-2,6-naphthalate) during crystallization from the melt. *Polymer* 1998;39:6325–30.
- [77] Kimura T, Kawai T, Sakamoto Y. Magnetic orientation of poly(ethylene terephthalate). *Polymer* 2000;41:809–12.
- [78] Ebert F, Thurn-Albrecht T. Controlling the orientation of semicrystalline polymers by crystallization in magnetic fields. *Macromolecules* 2003;36:8685–94.
- [79] Robelin-Souffache E, Rault J. Origin of the long period and crystallinity in quenched semicrystalline polymers. *Macromolecules* 1989;22:3581–94.
- [80] Kitamaru R, Horii F. Proton magnetic-resonance studies of phase structure of bulk-crystallized linear polyethylene. *Adv Polym Sci* 1977;15:821–36.
- [81] Strobl G, Hagedorn W. Raman spectroscopic method for determining the crystallinity of polyethylene. *J Polym Sci Polym Phys Ed* 1978;16:1181–93.
- [82] Wunderlich B. Reversible crystallization and the rigid-amorphous phase in semicrystalline macromolecules. *Prog Polym Sci* 2003;28:383–450.
- [83] Schick C, Wurm A, Mohamed A. Vitrification and devitrification of the rigid amorphous fraction of semicrystalline polymers revealed from frequency-dependent heat capacity. *Colloid Polym Sci* 2001;279:800–6.
- [84] Lin J, Shenogin S, Nazarenko S. Oxygen solubility and specific volume of rigid amorphous fraction in semicrystalline poly(ethylene terephthalate). *Polymer* 2002;43:4733–43.
- [85] Kristiansen P, Hansen E, Pedersen B. Isothermal crystallization of polyethylene monitored by in situ NMR and analyzed within the ‘Avrami’ model framework. *Polymer* 2001;42:1969–80.
- [86] Hertlein C, Saalwaechter K, Strobl G. Employing NMR in studies of polymer crystallization kinetics. *Polymer*; in press.
- [87] Strobl GR. *The physics of polymers*. Berlin: Springer; 1997. p. 185–8.
- [88] Hu W, Albrecht T, Strobl G. Reversible surface melting and crystallization of PE and PEO crystallites indicated by TMDSC. *Macromolecules* 1999;32:7548–54.

- [89] Albrecht T, Armbruster S, Keller S, Strobl G. Dynamics of surface crystallization and melting in polyethylene and poly(ethylene oxide) studied by temperature-modulated DSC and heat wave spectroscopy. *Macromolecules* 2001;34: 8456–67.
- [90] Tanabe Y, Strobl G, Fischer E. Surface melting in melt-crystallized linear polyethylene. *Polymer* 1986;27:1147–53.
- [91] Hobbs J, Humphris A, Miles M. In-situ atomic force microscopy of polyethylene crystallization. 1. Crystallization from an oriented backbone. *Macromolecules* 2001;34:5508–19.
- [92] Okui N, Umemoto S. Maximum crystal growth rate and its corresponding state in polymeric materials. In: Reiter G, Sommer JU, editors. *Polymer crystallization, Lecture notes in physics*. Berlin: Springer; 2003. p. 343–65.